FACULTY
OF MATHEMATICS
AND PHYSICS
Charles University

MASTER THESIS

Bc. Petr Král

Unconventional behavior of Ce and Yb compounds induced by extreme pressure

Department of Condensed Matter Physics

Supervisor of the master thesis: RNDr. Jiří Prchal, Ph.D.

Study programme: Physics of Condensed Matter and Materials

Specialization: Physics of atomic and electronic structures

Prague 2020

I declare that I carried out this master thesis independently, and only with the cited sources, literature and other professional sources.

I understand that my work relates to the rights and obligations under the Act No. 121/2000 Coll., the Copyright Act, as amended, in particular the fact that the Charles University has the right to conclude a license agreement on the use of this work as a school work pursuant to Section 60 paragraph 1 of the Copyright Act.

In Benešov 27.5.2020 Bc. Petr Král

In this place, I would like to express my gratitude to everyone, who supported me during my studies and to those without whom this work would not have arisen.
My greatest thanks belong to my supervisor RNDr. Jiří Prchal, Ph.D. for his willing and patient leading me throughout all work on my thesis, for motivation and for his support during many experiments, giving me valuable advice and devoting me time, whenever I needed.
I wish also to thank my advisor RNDr. Jiří Kaštil, Ph.D. for guidance during experiments carried out in FZU, for help with data processing and for factual remarks to the text of my thesis.
My gratitude belongs also to RNDr. Milan Klicpera, Ph.D. for preparing the single crystalline sample and for discussion about obtained data.
Then, I wish to thank doc. RNDr. Martin Diviš, CSc. for discussion about the theoretical background of the problematics of the thesis.
Last but not least, my thanks belong to all members of our department for practical help and useful discussions, especially Mgr. Kristina Vlášková for help with characterization of the samples and RNDr. Petr Doležal for help with the low temperature X-ray diffraction experiment.
Finally, I would like to thank my family and my girlfriend for their support, understanding and patience during my whole study.

Title: Unconventional behavior of Ce and Yb compounds induced by extreme pressure

Author: Petr Král

Department: Department of Condensed Matter Physics

Supervisor of the master thesis: RNDr. Jiří Prchal, Ph.D., Department of Condensed Matter Physics

Abstract: Thanks to the specific electronic structure the rare earth-based compounds, especially those containing Yb, Ce or Eu, often exhibit exceptional magnetic properties. In our study we have focused on cerium-based compound Ce_2Pd_2In belonging to the family of R_2T_2X compounds crystallizing in Mo_2FeB_2-type structure. Previous studies revealed presence of two magnetic phase transitions ($T_C \approx 4.1$ K and $T_N \approx 4.5$ K) and strong dependence of magnetic ground state on the changes of chemical composition. We carried out detailed ambient pressure characterization so as to expand our knowledge about this interesting system and to refine some previous results, especially the positions of phase transitions were newly determined as $T_C \approx 4.16$ K and $T_N \approx 4.65$ K and Ce magnetic moment was found to reach the value of 1.87 μ_B/Ce. However, the main tool used in frame of the thesis is application of mechanical pressure (both hydrostatic and uniaxial) which allows us to affect the interatomic distances and thus also the related physical properties without the composition change. It was found that antiferromagnetic phase remains to significantly lower temperatures under applied pressure, while changes in T_N are not so significant. Both types of pressure lead to lowering of Ce magnetic moment due to possible Kondo interaction.

Keywords: rare-earth intermetallics, Ce_2Pd_2In, magnetic state, hydrostatic pressure, uniaxial pressure

Contents

Introduction **1**

1. Theoretical background **2**

1.1. Rare earth element-based intermetallic compounds 2

1.2. Magnetism 3

1.2.1. Magnetism of free ions 3

1.2.2. Interactions between magnetic moments 7

1.3. Electric transport properties 10

1.4. Specific heat 13

1.5. Mechanical pressure 14

1.5.1. Description of the pressure 15

1.5.2. Effects of hydrostatic pressure on material properties 15

2. Experimental methods **17**

2.1. Preparation of samples 17

2.2. Diffraction techniques 17

2.3. Electron microscopy 18

2.4. Measurement of transport properties 19

2.5. Measurement of magnetic properties 20

2.6. High pressure experiments 21

3. Previous results and motivation **25**

3.1. Ce_2Pd_2In 25

4. Results and discussion **28**

4.1. X-ray powder diffraction 28

4.2. Ambient pressure characterization 31

4.2.1. Heat capacity 33

4.2.2. Electrical resistivity 35

4.2.3. Magnetization 37

4.2.3. AC magnetic susceptibility 46

4.3. Application of hydrostatic pressure 49

4.3.1. Electrical resistivity 49

4.3.2. AC magnetic susceptibility 52
4.3.3. Magnetization 54
4.3.4. Phase diagram 58
4.4. Application of uniaxial pressure 60
4.4. Discussion 64

Conclusion **68**

Bibliography **70**

List of Tables **73**

List of Abbreviations **74**

Introduction

Study of rare earth element-based compounds is in foreground of interest of condensed matter physics. Especially compounds containing Yb, Ce or Eu often exhibit interesting behavior such as non-integer valence or valence fluctuations [1, 2]. These are the well-known phenomena that are intensively studied both experimentally and theoretically [3-5]. The changes of valence can be accompanied for example with the onset of magnetism (or with its suppression) or with structure transitions (because the valence relates to the effective atomic radius).

In frame of this master thesis, we focused on Ce_2Pd_2In compound. Cerium-based intermetallic compounds attract much attention due to their anomalous physical behavior. It is predominantly governed by interactions of Cerium 4*f* electrons with non-*f* electrons of atoms in their neighborhood. This phenomenon is called *f*-ligand hybridization. The *f*-ligand hybridization is known to be very sensitive to external factors like magnetic field, pressure or to changes in atomic surroundings caused by hydrogenation – insertion of hydrogen atoms [6]. The main method we used for affecting the physical properties of chosen compound is application of mechanical pressure.

The thesis is divided into four main chapters. The first chapter introduces the theoretical background which is important to understand the physics behind observed sample properties. In the second chapter, the list of used experimental techniques with explanation of their principles is provided. In the next chapter, the motivation to our work and the previous results are dealt with. Most important is the fourth chapter containing our results discussed on the basis of the theory and previous results. The summary of obtained results is given in the conclusion.

1. Theoretical background

1.1. Rare earth element-based intermetallic compounds

Rare earth elements (*RE*s) is the collective name for the group of 17 chemically similar elements. This similarity originates in their common form of electron configuration [Xe] $6s^2\ 5d^1\ 4f^N$ for N going from 0 (La) to 14 (Lu). Number of 4*f*-electrons does not change (with few exceptions) even in the metallic state, because the spatial extent of 4*f* wave function ($\approx$ 50 pm) is smaller than the typical interatomic distance between two *RE* atoms and 4*f* functions are shielded by fully occupied 5*s* and 5*p* shells (the character of 4*f*-electrons is rather localized, as it can be seen in Figure 1.1), that's why it does not participate on metallic bonding. On the contrary, electrons from 6*s* and 5*d* shell participate on the bonding and consequently the most typical valence state of *RE* in the intermetallic compound is 3+.

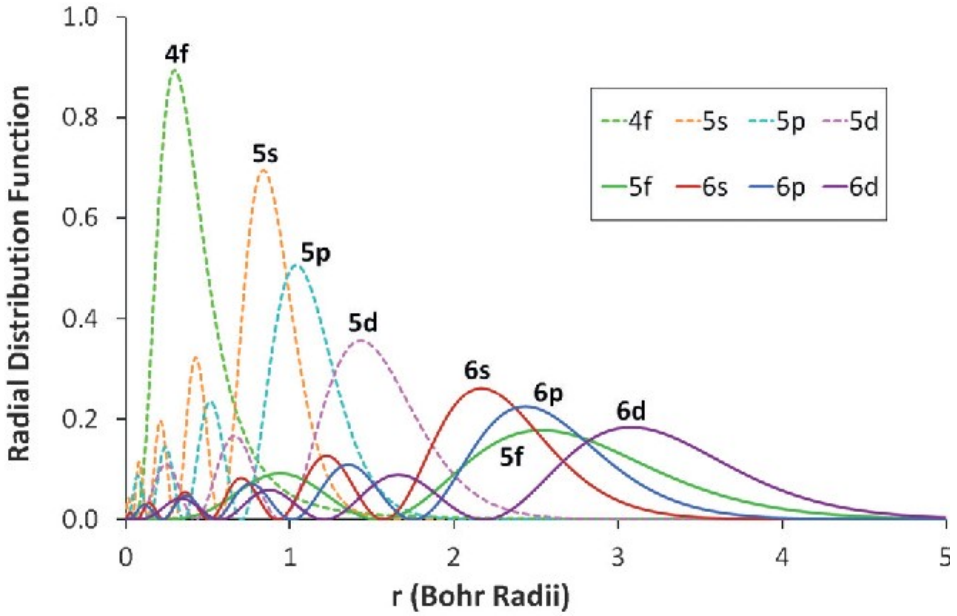

Figure 1.1: Radial distribution function of several electron orbitals. Picture taken from [7]

The 4*f*-level is not directly influenced by neighboring atoms, the states of 4*f* electrons are influenced by other 4*f* electrons and by the charge of nucleus shielded by inner electron shells (the effective charge of such nucleus can be written as $+\tilde{Z}e$). The total Hamiltonian of the system is then

$$\hat{\mathrm{H}}_{4f} = \sum_{i=1}^{N}\left(-\frac{\hbar^2}{2m_e}\right)\Delta_i + \sum_{i=1}^{N} -\frac{\tilde{Z}e^2}{r_i} + \sum_{i>j}\frac{e^2}{r_{ij}} + \hat{\mathrm{H}}_{\mathrm{SO}}\,. \tag{1.1}$$

The most interesting are intermetallic compounds containing Eu, Yb or Ce, due to their possible valence variations unlike other *RE* elements. Ytterbium has got nearly full filled 4*f* shell, only one electron is missing and two valence states are possible – classical 3+ state, in which Yb ion is magnetic, as it will be shown in subchapter 1.2., or non-magnetic state 2+, if one of the valence electrons fills the last place in the 4*f* shell – the shell is then fully filled. On the other hand, Cerium contains just one electron in its 4*f* shell, that's why it is possible to consider both elements as counterparts to each other. It can occur in magnetic state 3+ or in non-magnetic state 4+, when the only electron from 4*f* shell slides to valence layer, so the 4f shell results in empty one. Another mentioned element is Europium with possible valence states 3+ and 2+. In case of 3+ state, the total momentum J and thus also the magnetic moment according to (1.4) are equal to zero.

In compounds, mentioned *RE*s can occur in one of these valence states or as ions with an intermediate valence. This can be caused by two reasons – one of them is the presence of *RE*s in the both of valence states and the whole system appears as a mixture with some average valence, the second possibility is a presence of valence fluctuations.

1.2. Magnetism [8-10]

Magnetic properties of condensed matter are well described by quantum theory. Origin of magnetism in materials is in magnetic moments of the magnetic ions present in the sample, the interactions between magnetic moments and in the interaction of the localized 4*f* electrons with the crystal field.

1.2.1. Magnetism of free ions

The fundamental object in magnetism is the magnetic moment μ. The elementary magnetic moment $\mathrm{d}\mu$ of the closed current loop with the small area $\mathrm{d}S$ and the current I is given as

$$\mathrm{d}\mu = I\mathrm{d}S. \tag{1.2}$$

The direction of magnetic moment is normal to the loop. When the charge carriers are electrons with the particular mass, there exists the angular momentum L. Quantum mechanics introduces another momentum, the proper magnetic momentum of non-orbital origin called spin S. Due to this, it is possible to ascribe the magnetic momentum to every particle with non-zero spin, even if this particle would not have magnetic moment in classical physics (for example neutron, the particle without the electric charge). Magnetic moment of free ion is thus given by the current loop of the particle (electron) with the consideration of two contributions

$$\begin{aligned} \mu_L &= -L\mu_B \,, \\ \mu_S &= -Sg_0\mu_B \,, \end{aligned} \tag{1.3}$$

where $\mu_B = -\frac{e\hbar}{2m_e} = 9.27410 \cdot 10^{-24}\ \mathrm{JT}^{-1}$ stands for Bohr magneton and $g_0 \approx 2$ is g-factor of a free electron. According to the rules of momenta folding, the resulting magnetic moment of the 4*f* electron can be written as

$$\mu = -g\mu_B J, \tag{1.4}$$

where J is the total angular momentum and g is Landé g-factor given by equation

$$g = 1 + \frac{J(J+1) + S(S+1) - L(L+1)}{2J(J+1)}. \tag{1.5}$$

Localized model of free ion magnetism

According to the equation (1.4), the existence of non-zero angular momentum J is necessary for the formation of the magnetic moment.

Occupation of 4*f* electron states by electrons is given by the tendency to minimize the Coulomb interaction and the spin-orbit interaction energy in 4*f* shell. The ground state multiplet of lowest energy can be found by Hund's rules:

1. Maximization of the spin momentum S in accordance with the Pauli exclusion principle (according to this principle, every two electrons have to differ at least in one quantum number)
2. Maximization of the orbital momentum L in consistency with the first rule
3. The total momentum is given by

$$J = |L - S|, \qquad J = L + S \tag{1.6}$$

for the shell filled less than half and for the shell filled more than half, respectively.

The Hamiltonian of an atom with n electrons placed into the external magnetic field described by intensity H can be written as

$$\hat{\mathrm{H}} = \hat{\mathrm{H}}_0 + \mu_B\left(\hat{L} + 2\hat{S}\right)H + \frac{e^2}{8m_e c^2}H^2 \sum_{i=1}^{N}(x_i^2 + y_i^2)\,, \tag{1.7}$$

where x_i and y_i are the coordinates of electron i. Hamiltonian $\hat{\mathrm{H}}_0$ can be considered to play dominant role and the other parts can be counted by the perturbation theory of the second order. The resulting difference in energy is then given as

$$\Delta E = \mu_B\langle n|\hat{L} + 2\hat{S}|n\rangle H + \sum_{n'\neq n}\frac{\left|\langle n|\mu_B\left(\hat{L} + 2\hat{S}\right)H|n'\rangle\right|^2}{E_n - E_{n'}} + \frac{e^2}{8m_e c^2}H^2\langle n|\sum_{i=1}^{N}(x_i^2 + y_i^2)\,|n\rangle\,. \tag{1.8}$$

The third term of ΔE describes the diamagnetic contribution. It is dominant for ions with all shells fully filled in the ground state $|0\rangle$ when other terms vanish. It reflects the effort of electrons to shield inner parts of atom from the external field. Assuming the material with the volume V consisting of N identical non-interacting ions, we can write the so-called Larmor diamagnetic susceptibility as

$$\chi_{dia} = -\frac{N}{V}\frac{\partial^2 \Delta E}{\partial H^2} = -\frac{e^2}{6m_e c^2}\frac{N}{V}\langle 0|\sum_i r_i^2\,|0\rangle\,. \tag{1.9}$$

In this case, the diamagnetic susceptibility does not depend neither on temperature nor on external field.

When there is the situation of not fully filled shells, the diamagnetic contribution is very small compared to the first two terms in ΔE that describe paramagnetic contributions.

For the total momentum $J = 0$ the first of them vanishes (using Wigner-Eckart theorem for the ground state multiplet, we can write $\langle \hat{L} + 2\hat{S} \rangle = g\langle \hat{J} \rangle$) and the second one gives van Vleck paramagnetism. The van Vleck susceptibility is then given by

$$\chi_{Vleck} = \frac{2N\mu_B^2}{V} \sum_n \frac{\left| \langle 0 | H(\hat{L} + 2\hat{S}) | n \rangle \right|^2}{E_0 - E_n} \tag{1.10}$$

and it is also temperature independent.

For $J \neq 0$, the first term does not vanish and it is much bigger than other terms. Such an atom has got its own magnetic moment according to (1.4). For non-interacting ions, given temperature T and negligible crystal field, it is possible to write magnetization as

$$M = \frac{N}{V} g\mu_B J B_J \left(\frac{g\mu_B HJ}{k_B T} \right), \tag{1.11}$$

where B_J is the Brillouin function and $k_B = 1.38062 \cdot 10^{-23}$ JK^{-1} is the Boltzmann constant. In the limit of low temperatures and high fields, Brillouin function approaches constant value of 1 and that's why the magnetization does not depend on temperature. On the contrary for high temperatures and low fields, the function can be approximated by linear function. Then the magnetization can be written as

$$M \to \frac{N}{V} g^2 \mu_B^2 \frac{J(J+1)}{3k_B T} H \tag{1.12}$$

and it gives the relation for susceptibility known as Curie law

$$\chi = \frac{M}{H} = \frac{N}{V} g^2 \mu_B^2 \frac{J(J+1)}{3k_B} \frac{1}{T} = \frac{C}{T}, \tag{1.13}$$

where C is the Curie constant.

Curie constant can be rewritten into the following form:

$$C = \frac{\mu_0 N_A \mu_{eff}^2 \mu_B^2}{3k_B}, \tag{1.14}$$

where $N_A = 6.02217 \cdot 10^{23}$ mol^{-1} is the Avogadro's constant.

In previous part, there appears the expression $g^2J(J+1)\mu_B^2$, which has the meaning of effective magnetic moment squared μ_{eff}^2. Effective magnetic moment is thus given by

$$\mu_{eff} = g\sqrt{J(J+1)}\mu_B \tag{1.15}$$

and it can be calculated for free ions with given valence state.

1.2.2. Interactions between magnetic moments

Magnetic moments in the matter can interact with each other and their interaction can lead to the long-range magnetic ordered state. There are two main types of interactions – the magnetic dipole interaction and the exchange interaction.

Magnetic dipole interaction is very weak, and it can lead to magnetic ordered state only in very low temperatures (order of mK).

The second type is the exchange interaction.

The Hamiltonian of the exchange interaction can be expressed according to the Heisenberg model as

$$\hat{\mathrm{H}}_{\mathrm{ex}} = -\frac{1}{2}\sum_{i,j} J_{ij}\hat{S}_i\hat{S}_j\,, \tag{1.16}$$

where J_{ij} stands for the exchange integral, describing the interaction between spins of two electrons i and j.

It is possible to rewrite previous Hamiltonian as

$$\hat{\mathrm{H}}_{\mathrm{ex}} = -\sum_i \mu_i H_m\,. \tag{1.17}$$

Here $H_m = \sum_{i\neq j} \nu_{ij}\langle\mu_j\rangle = \nu\sum_{i\neq j}\langle\mu_j\rangle = \nu M$ ($\langle\mu_j\rangle$ is the statistical thermal average of moment μ_j, M is the magnetization, ν_{ij} contains the exchange integral J_{ij} and necessary constants and it is expected to be the same for all pairs of spins) is the effective Weiss molecular field.

The total magnetization can be written as $M = (H + H_m)\chi$ and from that it is possible to derive the Curie-Weiss law

$$\chi = \frac{M}{H} = \frac{C}{T - \theta_P}, \tag{1.18}$$

where $\theta_P = \nu C$ represents so called paramagnetic Curie temperature.

Exchange interactions can be divided into two groups.

First of them is the direct exchange interaction, which is typical for *d*-elements, light 5*f*-elements and their intermetallic compounds with sufficient overlap of appropriate wave functions of neighboring atoms with magnetic moment.

The second option is the indirect exchange interaction. In this case, the interaction between ions with magnetic moments is mediated by interaction with valence states of non-magnetic ligands – super-exchange (it prevails for example for some oxides of transition metals), or by conduction electrons – the RKKY (Ruderman-Kittel-Kasuya-Yoshida) interaction. In case of RKKY interaction, the localized magnetic moment polarizes conduction electrons in its vicinity and the information can be transferred over the long distance. This interaction is typical for 4*f*-metals and 4*f*-intermetallics. The RKKY exchange integral can be written as

$$J_{RKKY} \propto \frac{\cos(2k_F r)}{r^3}. \tag{1.19}$$

All of these interactions are schematically shown in following Figure 1.2.

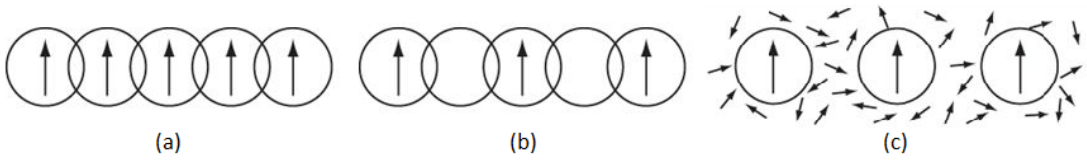

Figure 1.2: Magnetic exchange interactions: (a) Direct exchange, (b) Indirect Super-exchange, (c) Indirect RKKY interaction. Picture taken from [8]

Magnetic order

Above mentioned interactions are affecting magnetic moments of atoms in the matter. It depends on many factors, if these interactions cause the magnetic order. Against them act for example thermal fluctuations of spin mean values. On the other hand, magnetic order is energy efficient.

For description of some magnetically ordered state, it is possible to use Néel sublattices theory. In the system with long-range order, there exist the sublattices. Interactions can be then divided into the intra-lattice and inter-lattice ones. Sublattices can be chosen to be ferromagnetic. Then the intra-lattice exchange integral is positive, and the total order state is dependent on the sign of inter-lattice integral. There exist a lot of types of magnetic order, such as ferromagnetism, antiferromagnetism, ferrimagnetism or more complicated spiral or helicoidal. The latter two cannot be described by Néel sublattices theory.

Ferromagnetism

Ferromagnetic materials exhibit non-zero (so-called spontaneous) magnetic moment even without application of external magnetic field for temperatures below Curie temperature T_C. This temperature separates unordered paramagnetic phase for $T > T_c$ and ordered ferromagnetic state for $T < T_c$.

Antiferromagnetism

In the simplest case, there are two ferromagnetic sublattices oriented antiparallel to each other, the exchange integral is negative. The magnitude of magnetic moments in each sublattice is the same. That's why the total magnetic moment of the bulk is zero. For such materials the temperature of ordering is called Néel temperature T_N.

Ferrimagnetism

It is the special case of previous (antiferromagnetism) with the difference that the magnitudes of moments in different sublattices are not equal in ferrimagnetic materials. The resulting spontaneous magnetic moment is non-zero. Ferrimagnetism occurs for example in materials containing two elements with different non-zero magnetic moments.

Itinerant model of magnetism

Magnetic properties can have origin also in the magnetic moments of conduction electrons, which are not localized. In metals, electrons form the band structure which

can be under certain conditions split according to the spin. This phenomenon leads to non-zero magnetization.

Band structure can be split by external magnetic field, in following denoted as B, leading to the so-called Pauli paramagnetism. The magnetization is than given by following formula

$$M = \mu_B(\mathrm{DOS}_\uparrow - \mathrm{DOS}_\downarrow) = \mu_B^2 \mathrm{DOS}(E_F)B = \frac{3N\mu_B^2 B}{2k_B T_F}, \tag{1.20}$$

where $\mathrm{DOS}_\uparrow$ and $\mathrm{DOS}_\downarrow$ describe density of states with spin parallel and antiparallel to external magnetic field respectively, $\mathrm{DOS}(E_F)$ stands for density of states on Fermi level.

In terms of the spontaneous ordering and the itinerant model of magnetism, the Stoner criterion can be introduced. It says that the spontaneous splitting of bands followed by origin of ordered ferromagnetic state is possible, when the following criterion is fulfilled (I is so called Stoner parameter)

$$I\mathrm{DOS}(E_F) > 1\,. \tag{1.21}$$

1.3. Electric transport [8, 11]

The electrical resistivity is the fundamental property of materials that express how strongly the material opposes the flow of electric-charge carriers. It is caused by scattering of conduction electrons on scattering centers of various origins.

According to the Matthiessen's rule the total resistivity can be expressed as the sum of individual contributions. That's why it can be written as

$$\rho_{tot}(T) = \rho_R + \rho_{phonon}(T) + \rho_{mag}(T). \tag{1.22}$$

Here ρ_R is temperature independent contribution called residual resistivity which is caused by scattering of electrons on various defects of the lattice (point defects such as vacancies or interstitials, line defects, mainly dislocations, planar defects such as grain boundaries, twin boundaries or bulk defects, for example impurity phases).

The second term represents scattering electrons on phonons (lattice vibrations). This contribution depends on temperature and it can be described by Bloch-Grüneisen formula

$$\rho_{phonon}(T) = 4R_{\Theta}\left(\frac{T}{\Theta}\right)^5 \int_0^{\frac{\Theta}{T}} \frac{x^5}{(e^x - 1)(1 - e^{-x})}\,\mathrm{d}x\,, \tag{1.23}$$

where R_{Θ} is the parameter and Θ stands for the Debye temperature. In the limit of high temperature, the phonon contribution behaves as $\rho_{phonon}(T) \propto T$ and for low temperatures as $\rho_{phonon}(T) \propto T^5$.

Last term in (1.22) expresses the dependence of electrical resistivity on magnetic state of the material due to interaction of conduction electrons with magnetic moments in the matter. In paramagnetic region and the negligible crystal field and spin fluctuations, the moments are not ordered and the contribution to the electrical resistivity does not depend on temperature. Below the ordering temperature it starts to be temperature dependent. Generally, it can be said that in the consequence of magnetic ordering the resistivity is decreasing.

The temperature dependence of individual contributions and the total electrical resistivity are shown in following Figure 1.3.

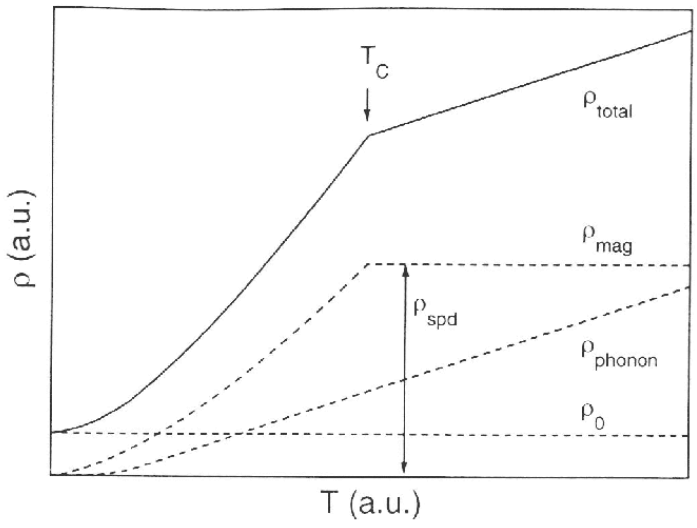

Figure 1.3: Individual contributions to the electrical resistivity and the total curve given as the sum of them. Picture taken from [11]

Some compounds may exhibit the increase of electrical resistivity below the characteristic temperature – so called Kondo temperature. This effect has origin in a

Kondo screening [8]. It is based on the interaction between the spin of conduction electrons and the total angular momentum of magnetic atoms. Conduction electrons can form the cloud that screens the magnetic moment of an atom. In such case, the additional contribution to the electrical resistivity can be described as

$$\rho_{Kondo} \propto \ln\left(\frac{1}{T}\right). \tag{1.24}$$

The typical behavior of electrical resistivity when Kondo interaction is present at low temperatures (Au matrix with small amount of Fe-impurities) is shown in following Figure 1.4.

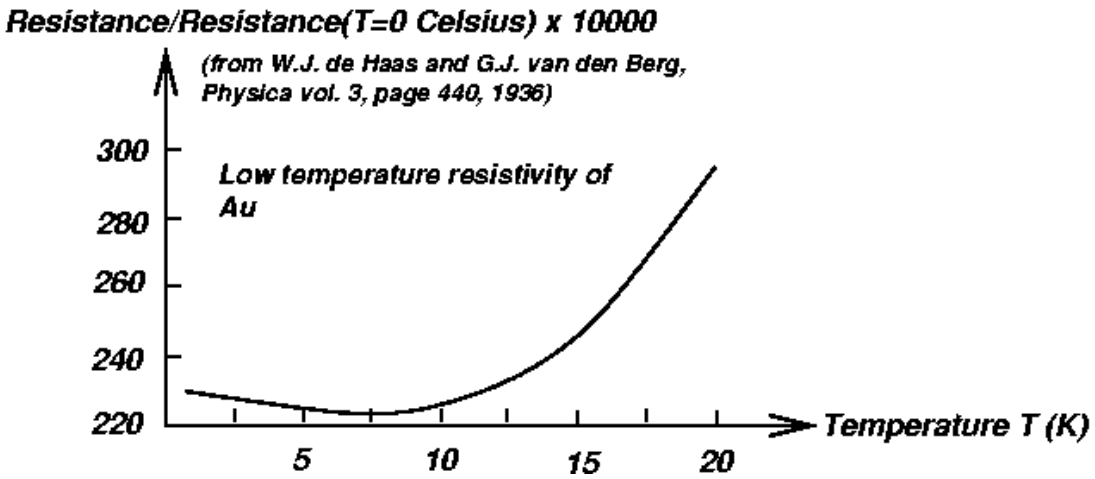

Figure 1.4: Electrical resistivity with characteristic increase in low temperature in presence of Kondo interaction. Picture taken from [12]

In an experiment we usually measure the electrical resistance R. It is connected with the electrical resistivity through the shape factor. It is given by the formula

$$R = \frac{\rho l}{S}, \tag{1.25}$$

where S stands for the area of cross section of the sample and l is the distance of two voltage contacts (resistance is usually measured by four wire method with two current and two voltage contacts).

The low temperature region of measured curves for correlated electron systems can be fitted by

$$\rho = AT^n + \rho_R\,, \tag{1.26}$$

where ρ_R stands for the residual resistivity and the value of exponent n differs according to the kind of behavior of the particular material. Value $n \approx 2$ is typical for

Fermi-liquid behavior, while $3/2 < n < 2$ indicates non-Fermi-liquid behavior of the sample [13].

1.4. Specific heat

This physical quantity is defined as the heat energy, which is needed to raise the temperature of the sample of unit mass by 1 K. According to the conditions of experiment, the specific heat is given as

$$C_X = \left(\frac{\delta Q}{\mathrm{d}T}\right)_X , \tag{1.27}$$

where X stands for the parameter that is fixed during the experiment. Typically, it is the volume resulting in C_V or the pressure giving C_p, which is usually measured because of the easier holding of constant pressure in comparison with the volume.

The total specific heat of the material can be written as the sum of individual contributions

$$C_p^{tot} = C_{ph} + C_{mag} + C_{sch} + C_{el} + C_n , \tag{1.28}$$

where C_{ph} stands for the phonon contribution, C_{mag} and C_{sch} are connected with magnetic interactions and crystal field contribution, respectively, C_{el} is the contribution of conduction electrons and C_n represents the contributions from atomic nuclei.

The temperature dependence of heat capacity can be also used for determination of phase transition temperature. In terms of the second order phase transitions, the method of idealization of transition according to specific heat while maintaining the entropy can be applied. When the transition is of the second order, the first derivatives of Gibbs free energy like entropy or volume are continuous. The discontinuity appears in the second derivatives, for example right in heat capacity. The method is based on following thermodynamic relations. Let us deal with the case of constant volume of the sample. From the first law of thermodynamics the heat given into thy system can be written as

$$\delta Q = T\mathrm{d}S. \tag{1.29}$$

Using this equation, the heat capacity can be rewritten as

$$C_p = \frac{\delta Q}{\mathrm{d}T} = \frac{\mathrm{d}H}{\mathrm{d}T} = T\left(\frac{\mathrm{d}S}{\mathrm{d}T}\right)_p, \tag{1.30}$$

where H stands for the enthalpy. From the last equation it is clear, that the derivative $(dS/dT)_p$ is given as C_p/T. That's why the entropy is given as the integral of C_p/T, which is represented as the area in the plot of C_p/T as the function of T, by

$$S = \int_0^T \frac{C_p}{T'}\,\mathrm{d}T'. \tag{1.31}$$

In practice, we estimate the tangent to the data points below the transition as well as above it and then, we are searching the vertical line determining the temperature of transition. Its position has to fulfil the condition that the area bounded by the tangent, data points and the vertical line has to be the same below the transition and above it. This method was used for finding the critical temperatures in Ce_2Pd_2In. The process is shown in subchapter 4.2.1.

1.5. Mechanical pressure [14-16]

Magnetic interactions between magnetic moments in the condensed matter also depend on the distances between the magnetic atoms. There are several options how to affect the interatomic distances, namely by the temperature (due to the thermal expansion), by chemical substitution (replacement of one element with another one with different effective volume) or by external mechanical pressure. The advantage of the latter one compared to the chemical substitution lies in studying the same sample for the whole experiment. The substitution means using of different sample, i.e. matter with different chemical properties and also the electronic structure of the substituted compound. Another disadvantage is the fact that it is necessary to prepare several samples with given composition. Using the pressure allows us to avoid optimization process of preparation of samples with the new composition if only the change of interatomic distances is required. The temperature, on the other hand, changes neither the chemical nor the electronic structure, but it affects the degree of occupation of quantum states in studied compound.

1.5.1. Description of the pressure

Mechanical pressure is generally described as the force F acting on the surface S.

$$p = \frac{F}{S}. \tag{1.32}$$

For the accurate description of the pressure the stress tensor $\boldsymbol{\sigma}_{ij}$ is introduced, in cartesian coordinates the form is as following

$$\boldsymbol{\sigma} = \begin{pmatrix} \sigma_{11} & \sigma_{12} & \sigma_{13} \\ \sigma_{21} & \sigma_{22} & \sigma_{23} \\ \sigma_{31} & \sigma_{32} & \sigma_{33} \end{pmatrix}. \tag{1.33}$$

Diagonal components $\boldsymbol{\sigma}_{ii}$ stand for the direct stress in three orthogonal directions, while the non-diagonal elements represent the shear stress. Direct stress is normal to the surface and it tends to a volume change. The shear stress results in deformation of the sample shape without a volume change. Stress tensor is generally defined in every time and space point and the time and space dependent pressure can be defined as

$$p(\boldsymbol{r}, t) = -\frac{1}{3}\big(\sigma_{11}(\boldsymbol{r}, t) + \sigma_{22}(\boldsymbol{r}, t) + \sigma_{33}(\boldsymbol{r}, t)\big). \tag{1.34}$$

In a special case, when the non-diagonal elements of the stress tensor are zero and the diagonal components are equal (case of isotropic stress), we can introduce the hydrostatic pressure by formula

$$p(\boldsymbol{r}, t) = -\sigma_{11} = -\sigma_{22} = -\sigma_{33}\,. \tag{1.35}$$

1.5.2. Effects of hydrostatic pressure on material properties

Mechanical hydrostatic pressure applied on the sample leads to changes in sample properties. As mentioned above, the main reason is the fact, that pressure affects the interatomic distances in the matter. The lattice parameters can be increased or decreased, but the resulting volume decreases. The change in volume can be described by the isothermal compressibility

$$\kappa = -\frac{1}{V}\left(\frac{\mathrm{d}V}{\mathrm{d}p}\right)_T. \tag{1.36}$$

Compressibility of the material is in general decreasing with increasing the pressure ($\kappa \sim V^{5/3}$) while the volume decreases with increasing pressure. The same impact has

the pressure on the number of electrons on Fermi level ($N(E_F) \sim V^{2/3}$), while the Fermi energy is decreasing ($E_F \sim V^{-2/3}$).

Another physical quantity is the bulk modulus describing how strongly the material resists towards compression under pressure and it is defined as the inverse value to the isothermal compressibility

$$K = \frac{1}{\kappa}. \tag{1.37}$$

Mechanical pressure has also impact on electronic structure of the material. Increased pressure leads to enhancement of the overlap of atomic wave functions accompanied by the increase of values of overlap integrals. The electron bands are getting wider, the energy gaps can be reduced (it can affect other material properties – optical, electric conductivity and so on) at enhanced pressure. Pressure can also lead to the delocalization of electrons, also the binding character can be influenced (from ionic through covalent to metal bond with increasing the pressure).

Decrease of interatomic distances induced by pressure can affect the exchange interactions. Changes in the value of exchange integral J_{ij} have the impact on ordering temperatures and cause their shift. In compounds where RKKY interaction prevails, also the type of magnetic order can be affected because of the change in the sign of the exchange integral.

Application of pressure on superconducting materials usually leads to lowering of the transition temperature. This phenomenon is used in the secondary manometers for pressure determination in the pressure cell. As an example, the pressure dependence of superconducting transition in Pb is given as [17]

$$T_C(p) = T_C(0) - 0.0405p(\text{kbar}), \tag{1.38}$$

where $T_C(0) = 7.19$ K stands for the Pb superconducting transition in ambient pressure.

2. Experimental methods

2.1. Preparation of samples

Polycrystalline sample of Ce_2Pd_2In was prepared in arc furnace by using elements with high purity (Ce with purity 2N8 – purified by SSE (Solid State Electrotransport method), Pd with 4N5 and In with 5N) weighed in atomic ratio. The preparation process took place in a mono-arc furnace under the protective argon atmosphere. The mixture of elements was melted and then turned and remelted three times to ensure their homogeneity. Prepared sample was divided into two parts – one of them was checked in terms of homogeneity and phase purity and left as sufficiently suitable piece for other use. The second one was wrapped into the tantalum foil to avoid contacting the silica glass containing oxygen that can contaminate the sample, then sealed into a silica glass tube with protective argon atmosphere and annealed at 750°C for 10 days. After comparing the homogeneity and stoichiometry of the sample before and after annealing, we decided to use the annealed one for other measurements.

Single-crystalline samples were prepared by RNDr. Milan Klicpera, Ph.D. using the Czochralski growth method in tri-arc furnace. As the precursor, the polycrystalline sample of Ce_2Pd_2In prepared in mono-arc furnace was used. Then the samples were wrapped into the tantalum foil, as in the case of polycrystal, sealed in a glass tube and annealed at 750°C for 10 days.

2.2. Diffraction techniques [18]

The method usually used for characterization of the phase purity and crystal structure parameters of the sample is the X-ray powder diffraction. Principle of this method is the following. Monochromatic X-ray beam impacts the sample, and after diffraction on the sample the detector measures the intensity in dependence on the diffraction angle 2θ. The position of peaks in diffraction pattern is described by Bragg equation

$$2d_{hkl}\sin(\theta) = \lambda. \tag{2.1}$$

This equation describes which crystal planes d_{hkl} (h, k, l are Miller indices) can diffract for given X-ray wavelength λ and angle θ. Diffraction pattern is unique for each material and from its parameters (positions of peaks, their shape) it is possible to

find the number of phases, symmetry of their crystal lattice, lattice parameters, positions of atoms, texture, tension in the lattice or occupancy.

The measurement was carried out on powder diffractometer Bruker D8 Advanced in so called Bragg-Brentano θ-2θ geometry. The source of X-ray is Cu anode with the wave lengths $\lambda_{K\alpha 1} = 1.54050$ Å and $\lambda_{K\alpha 2} = 1.54434$ Å. Other wave lengths were eliminated from spectrum by monochromators.

Diffraction pattern was analyzed using FullProf software developed in ILL Grenoble [19]. It is based on Rietveld method. As the input it is necessary to insert the space group of studied crystal and the program is refining the parameters (for example scale, background, lattice parameters or coordinates of atoms) to fit the measured pattern with the least squares method.

Laue diffractometer PhotonicScience was used for orientation of chosen monocrystalline samples.

Laue method uses polychromatic X-ray radiation. The incident beam impacts the monocrystalline sample which has got the fixed position, it diffracts and then the distribution of intensity is detected. The fact that we use the polychromatic X-ray beam ensures that we detect sufficient number of Laue spots, although the experimental setup is static.

For low temperature X-ray powder diffraction serving to study the influence of temperature on lattice parameters, LT Diffractometer – D500-HR-4K equipped with a closed cycle cryocooler (101J Cryocooler ColdEdge) allowing to reach temperatures down to 3.2 K, was used. This diffractometer works with so called Brag-Brentano θ-θ geometry, the position of sample is not changed during measurement. Incident monochromatic beam impacts the powdered sample and it diffracts on the grains. In case of fulfilling the Bragg condition (2.1), a diffracted intensity appears and is detected by the detector.

2.3. Electron microscopy [20, 21]

Scanning electron microscope is the device which uses focused electron beam to image the sample. The primary electrons with energy of the order of 10 keV interact with the

sample in several different ways and according to the type of interaction we can detect secondary electrons, backscattered electrons or characteristic radiation.

Secondary electrons have their origin in inelastic scattering. Incident electron causes the release of an electron from the atom of studied sample. These electrons are then leaving the sample with low energy in comparison to the incident beam (< 50 eV). These electrons come from the thinnest layer of the sample and they provide the information about the topographical information.

On the other hand, the backscattered electrons come from the elastic scattering process, that's why their energy is comparable to energy of primary electrons. They provide the information about the composition of the sample because the probability of backscattering depends on atomic number.

Energy dispersive X-ray analysis (EDX) allows to study the chemical composition. Incident electron excites an electron from the inner shell and then we detect the characteristic X-ray radiation coming from following recombination to the ground state. The set of frequencies coming from these transitions between electron energy levels (characteristic radiation) is given by quantum theory and it is typical for each element.

All information provided by scanning electron microscope comes from the thin surface layer due to the low penetration depth and it is not possible to get information about composition of the whole sample.

The scanning electron microscope MIRA I Tescan was used to obtain the information about topography and chemical composition of studied samples.

2.4. Measurement of transport properties

Measurements of electrical resistivity and heat capacity were carried out in the Physical Property Measurement System (PPMS) by Quantum Design [22]. This device allows us to measure down to 2 K (with additional He3 option, we can reach 0.4 K) and to external magnetic field up to 9 T.

For electrical resistivity measurement, the sample is fixed by GE varnish (special glue suitable for low temperatures) to the special puck (on the electrically insulating pad) and it is contacted by four wires (two current and two voltage) to eliminate the influence of the wires on the value of the sample resistivity.

The heat capacity was measured also in the PPMS device [23]. In this case, the sample is attached to the special puck by the thin layer of Apiezon grease, which ensures thermal contact between the sample and the pad containing the heater and the thermometer on its bottom side. The measurement is realized by the relaxation heat-pulse method. Temperature of the sample is stabilized at given base temperature, then the heat-pulse is applied, and the temperature is increased. After that, the relaxation of the temperature in time is measured. The relaxation curve is analyzed by the PPMS software and it provides the information about the heat capacity value. We also used the long-pulse method, when the heat-pulse exceeds the longer temperature range and the heating curve itself presents the temperature dependence of the heat capacity. This method is time-saving and it was used for measurement of heat capacity of Ce_2Pd_2In in the temperature region around magnetic phase transitions.

Before measurement of the sample heat capacity itself, the contribution of Apiezon (the exact amount used to attach the sample later in the measurement) was measured. It is called addenda and it has to be together with the contribution of the whole puck subtracted from the total heat capacity to obtain the sample properties. All of the calculations are carried out by software.

2.5. Measurement of magnetic properties

To investigate the magnetization of the sample in the temperature region between 2 K and the room temperature and in magnetic fields up to 7 T, the Magnetic Property measurement System (MPMS) by Quantum Design was used [24]. This device is able to measure the smallest magnetic signal using the SQUID (superconducting quantum interference device) magnetometer. This device is based on the principle of the Josephson's junction and it allows us to detect magnetic flux passing through the superconducting coil even of the magnitude of one quantum given as $\Phi_0 = \frac{h}{2e} \approx 2.068 \cdot 10^{-15}$ Wb.

The measurement was carried out for orientation of external magnetic field with respect to two crystallographic directions – along [110]-axis and *c*-axis. The sample in the chosen orientation is fixed into the plastic straw by GE varnish and then put inside the device.

In the case of real non-ideal sample, it is necessary to calculate with the demagnetization field, which is generated by the magnetization of the sample. It leads to lowering the value of external magnetic field inside the sample as it is given by

$$H_{int} = H_{ext} + H_{demag} = H_{ext} - DM, \tag{2.2}$$

where D stands for so called demagnetization factor, which can be calculated in dependence on the shape of the sample. For example, for sample with shape of cube or sphere, we obtain $D = \frac{1}{3}$, ideal shape with $D = 0$ is the long cylinder with field applied along the axis of the cylinder or the plane with field direction lying in the plane, on the contrary the worst shape is the plane with field perpendicular to it. For more difficult shapes of samples, the calculation of demagnetization factor is difficult leading to difficult expressions. The case of rectangular prism is discussed in [25]. The formula for D derived there was used for calculation in our experiments [26].

2.6. High pressure experiments

Several types of pressure cells were used for application of the mechanical pressure. The choice depends on the physical property we intend to study or on the device used for measuring – it limits the suitable dimensions of the cell.

Hydrostatic double layer pressure cell

A double layer cylindrical pressure cell made of CuBe (outer layer) and NiCrAl (inner layer) with nominal pressure range up to 3 GPa [27] was used for measurement of electrical resistivity and AC magnetic susceptibility, both at the same time (in order to ensure the same conditions) under high pressure.

The sample of suitable dimensions is fixed to the thin paper by GE varnish. Four gold wires were used for four-point configuration method of electrical resistivity measurement to eliminate the influence of resistance of wires. Micro-welding was used

to make electrical contacts and also the silver paste was used to reinforce them because they are strained a lot during both preparation and duration of experiment. Then the sample was put into the system of coils with the inner diameter of 1.66 mm. This system consists of the excitation (200 turns) and detection (signal) coil with the compensation coil (50 + 50 turns) winded in opposite direction. The measured signal contains the induced voltage caused by the magnetic signal from the sample (detection part) with directly subtracted signal from the environment (compensation part without sample). Four resistivity wires were connected to the plug with the silver paste DuPont and the connection of four wires from coils and also manganin wire to the plug was realized by soldering. Thermally stabilized manganin wire serves for determination of the pressure at room temperature. For particular manganin wire the dependence of its resistance on the pressure can be described as

$$R(T,p) = R(T,0)(1 + \alpha(T)p), \tag{2.3}$$

where α is the pressure coefficient of resistance of manganin which was in our case $\alpha = 0.00246$ at room temperature. The pressure difference between the room- and the lowest measured temperature inside the pressure cell is $\Delta p \approx 0.3$ GPa and it remains similar all over the used range of pressures.

The whole measurement assembly is put inside the Teflon cell with the length of 21 mm and diameter 4 mm (outer) and 3 mm (inner).

All parts of the pressure cell are shown in the following Figure 2.1.

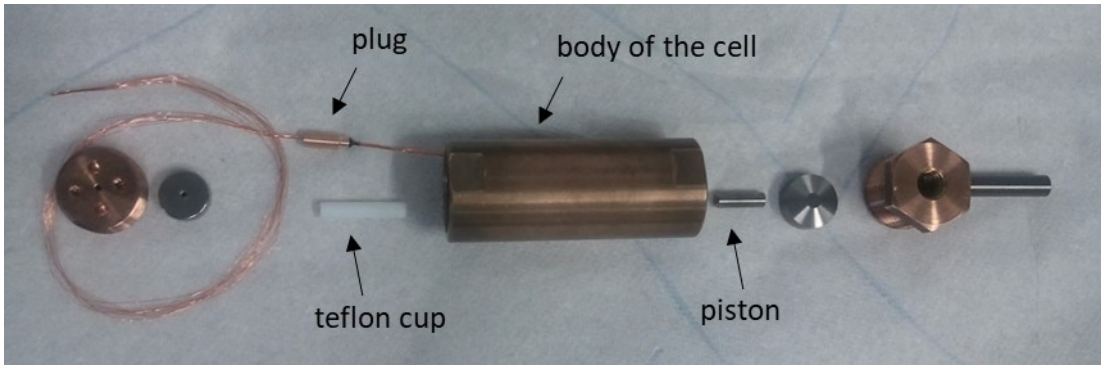

Figure 2.1: CuBe/NiCrAl double layer cylindrical piston hydrostatic pressure cell. Picture taken from [28]

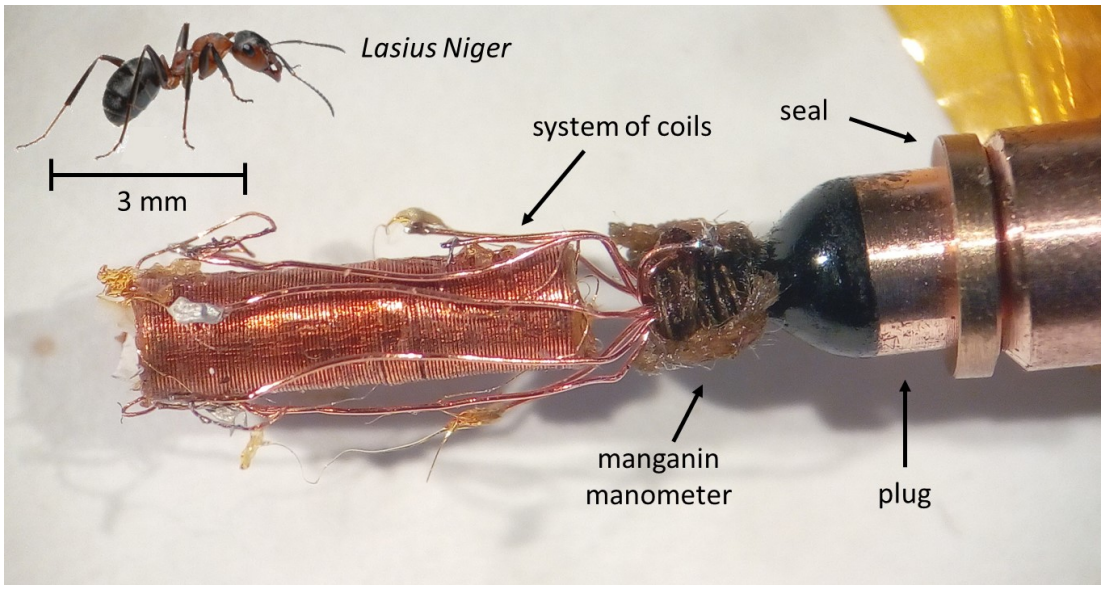

Figure 2.2: Preparation of the sample for measurement in pressure cell shown in Figure 2.1. For the better idea of size, the picture of an ant [29] is added to the figure

As a pressure-transmitting medium Daphne oils 7474 and 7575 were used [30, 31]. These media ensure the equal distribution of pressure (hydrostaticity) within the sample space of the pressure cell.

Hydrostatic pressure cell for magnetization measurement

The magnetization of the sample was measured in the CuBe hydrostatic pressure cell designed by Ing. J. Kamarád, CSc. (Institute of Physics, Academy of Sciences, [32]). It allows us to measure the magnetization in SQUID magnetometer MPMS for pressures up to 1 GPa. The cell is shown in the Figure 2.3. The sample is fixed by GE varnish in the chamber. As the pressure transmitting medium, Daphne oil 7373 was used [33]. The space filled by the medium is sealed by the series of seal rings. Finally, the pressure is realized by the piston pushed by tightening the screw. This pressure cell allows us to measure the pressure at low temperatures. The applied pressure is approximately settled at room temperature from the known number of turns of the screw and the exact value is determined according to the superconducting transition of lead (see subchapter 1.5.2.).

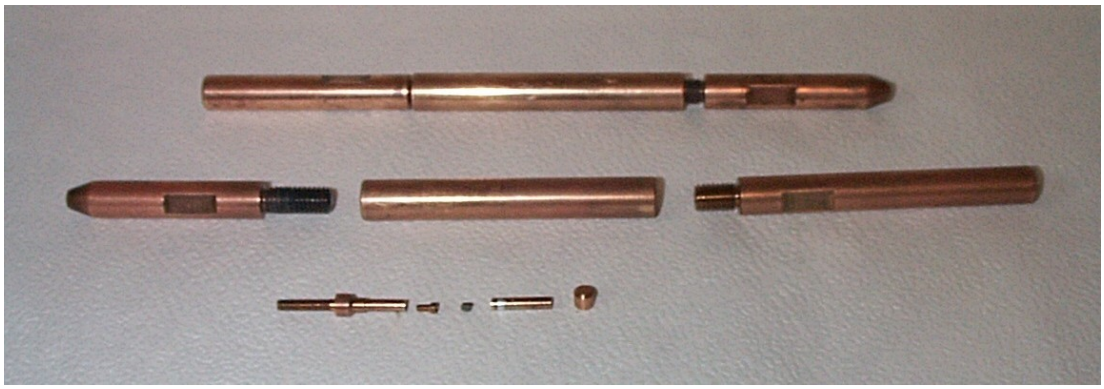

Figure 2.3: CuBe hydrostatic pressure cell for magnetization measurement

The uniaxial pressure cell

In order to apply the uniaxial pressure on the studied sample, the CuBe uniaxial pressure cell similar to the one mentioned in previous paragraph was used (Figure 2.4) [34]. This pressure cell allows to measure the magnetization in MPMS. Contrary to the hydrostatic pressure described in the previous paragraph, no exchange medium should be used as the pressure is uniaxial by wish in this case. Pressure is determined directly from the definition (1.32), where F stands for the force, which is given by number of screw turns – in the cell, there is the spring with defined stiffness, and S is the area of the sample. For this kind of experiment, the sample with dimensions approx. 1×1 mm and the thickness max. 200 μm is used.

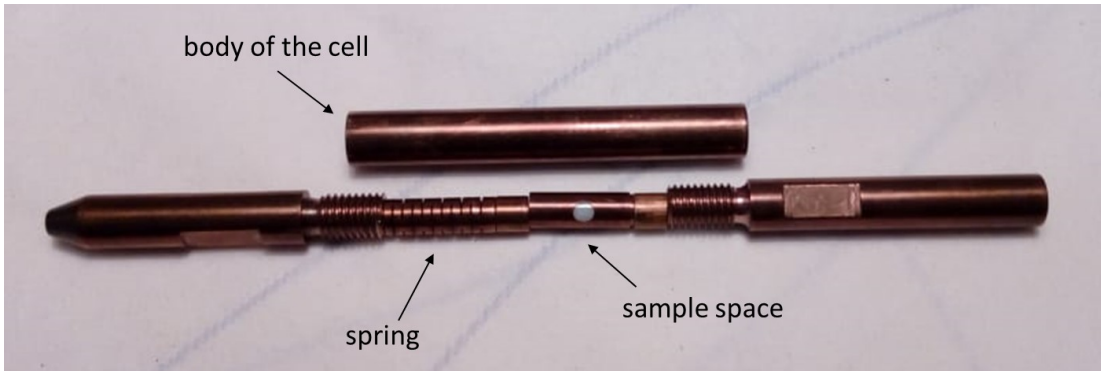

Figure 2.4: CuBe uniaxial pressure cell

3. Previous results and motivation

Numerous 2:1:2 intermetallic compounds belonging to R_2T_2X family (T stands for the transition metal, X for p-metal) crystallizing in tetragonal Mo_2FeB_2-type structure exist both for R = lanthanides and actinides [35]. This structure type is the ternary derivative of U_3Si_2 (space group 127: P4/*mbm*). This is a good opportunity to compare the appearing magnetism in 4*f* intermetallics with magnetism related to 5*f* states in actinide-based compounds. Materials based on actinides (U, Np, Pu) exhibit crossover from antiferromagnetic order to weak Pauli paramagnetism, when the hybridization between 5*f* states and ligand states gets stronger. On the other hand, 4*f*-element based compounds are mostly antiferromagnetic. The most typical interaction responsible for magnetic order in the latter case is RKKY interaction.

Interesting magnetic properties of such materials are related to the crystal structure. As it is shown in Figure 4.1, the lattice is formed by planes consisting of the rare earth elements with possible non-zero magnetic moment alternated by non-magnetic planes containing other elements. The rare earth atoms are forming triangular motif, which can, depending on the character of exchange interaction, bring the geometrical frustration into the system. This is equivalent to the two-dimensional Shastry-Sutherland lattice [36].

3.1. Ce_2Pd_2In

Discovery of U_2T_2X compounds (T stands for transition metal, X for In or Sn) crystallizing in the Mo_2FeB_2-type structure led to synthesis and characterization of the Ce counterparts. Several compounds with the formula Ce_2T_2X have been investigated and some of them exhibit interesting properties such as heavy fermion or Kondo behavior [37].

Depending on the character of *d*-band of transition metal T in Ce_2T_2In the compounds exhibit well-localized magnetism (Ce_2Cu_2In, Ce_2Pd_2In and Ce_2Au_2In) or valence fluctuations (T = Ni, Rh) [38, 39]. For Ce_2Pd_2X (X = In, Sn, Pb), there was observed magnetic ordering at low temperatures [37]. Among the group of R_2Pd_2In compounds, the Ce-based one exhibits the most interesting magnetic behavior. It reaches the ferromagnetic ground state below 4.1 K through an intermediate antiferromagnetic

phase [40-42]. Similar magnetic properties were observed in Ce_2Pd_2Sn, which reaches the ferromagnetic grounds state below 2.2 K also through an antiferromagnetic interphase [43].

Physical, especially magnetic, properties are strongly dependent on the interatomic distances in crystal lattice. In previous studies, the so called chemical pressure was applied in sense of changing the stoichiometry or by hydrogenation.

Hydrogen content up to 1.5 in $Ce_2Pd_2InH_x$ leads to ferromagnetic ground state, while for larger amount, up to x = 2.5, the compound orders antiferromagnetically. There were nevertheless CeH_2 and CePdIn impurities present in the sample for higher hydrogen content. With increasing of H content, almost linear and nearly isotropic expansion in both of lattice directions a and c was observed. Such behavior suggests that hydrogen atoms randomly occupy interstitial positions [6].

Magnetic ground state of Ce_2Pd_2In compound was also found to be very sensitive to the off-stoichiometry [44]. The excess of Ce at the expense of In in $Ce_{2+x}Pd_{1.85}In_{1-x}$ leads to ferromagnetic ground state, while the excess of Pd in $Ce_{1.95}Pd_{2+2x}In_{1-x}$ results in incommensurate sinusoidal modulated type of antiferromagnetism, which can be described by propagation vector $k \approx [0.22,0,0]$. The neutron diffraction data showed that the magnetic moments are in both cases (Pd-rich, Ce-rich composition) oriented parallel to the *c*-axis. The observed change in the magnetic ground state may be rationalized by the oscillating nature of RKKY exchange interaction. Both phase transitions are present in the case of accurate stoichiometry [40].

Another way, how to affect the interatomic distances, is application of mechanical pressure. As the most common exchange interaction in rare earth-based compounds is the RKKY interaction (for which the sign depends on the distance between magnetic ions), pressure poses the way, how to influence magnetic properties. Another feature that can be affected by pressure is the valence state of the rare earth element.

All of above mentioned results were obtained for polycrystalline samples. M. Klicpera et al. [40] dealt with studying of magnetic properties of single crystals with stoichiometry on slightly Pd-rich side. Investigation by means of X-ray diffraction, magnetization, specific heat and electrical resistivity was carried out and confirmed

the presence of two magnetic transitions. The ground magnetic state of this compound is ferromagnetic. Around temperature 4.1 K it changes into antiferromagnetic and then, around 4.5 K, there is the second phase transition to the paramagnetic state. Measurements of magnetization were carried out with field orientation along three directions – [100], [110] and [001]. Results for field along the basal plane directions are almost identical. On the other hand, a relatively strong anisotropy was observed using the third mentioned field direction (field along *c*-axis). The *c*-axis was found as an easy-axis of magnetization. It is in good agreement with above mentioned result of neutron diffraction [44]. Effective magnetic moment was found to be $\mu_{eff} = 2.38\,\mu_B/\mathrm{Ce}$ (close to Ce^{3+} free ion $\mu_{eff} = 2.54\,\mu_B/\mathrm{Ce}$). Also the obtained saturated magnetic moment $2.16\,\mu_B/\mathrm{Ce}$ for magnetization easy axis *c* is close to the value for free Ce^{3+} ion moment of $2.14\,\mu_B/\mathrm{Ce}$. Lower values obtained in some previous studies for polycrystalline samples [44] were considered as the consequence of averaging of randomly oriented grains with high uniaxial anisotropy in [40]. For paramagnetic Curie temperature, two values were obtained as the consequence of anisotropy. Their difference $\Delta\theta_P \approx 62$ K can be used to calculate the uniaxial anisotropy energy $\Delta E_A = k_B \Delta\theta_P \approx 5.3$ meV. Results given by magnetization and heat capacity measurements were compared to the first principle calculations and reasonable agreement was obtained. The Sommerfeld coefficient of electronic specific heat was estimated, using results of electrical resistivity measurement, as $\gamma = 50$ mJ mol^{-1} K^{-2}. This value is not enhanced enough to indicate the compound as heavy fermion ($\gamma > 400$ mJ mol^{-1} K^{-2}). In terms of two phase transitions, curves $M/H\ (T)$ are discussed in dependence on magnetic field. For higher values of field, transitions become less distinguished and they merge around 0.1 T, when the saturation is achieved for H along *c*. Measurements of electrical resistivity showed the difference between curves with different current direction for temperatures below 250 K, over this temperature, the resistivity values become quite isotropic.

4. Results and discussion

4.1. X-ray powder diffraction

The X-ray powder diffraction was used for determination of the crystal structure of the studied compound. We verified, that Ce_2Pd_2In crystallizes in expected tetragonal Mo_2FeB_2-type structure of space group P4/*mbm* (space group number 127). Diffraction patterns were processed using the FullProf software developed in ILL. Crystal structure of Ce_2Pd_2In compound is shown in Figure 4.1, which was obtained using the Vesta software. The room temperature lattice parameters were found to be $a = 7.801(2)$ Å and $c = 3.919(1)$ Å.

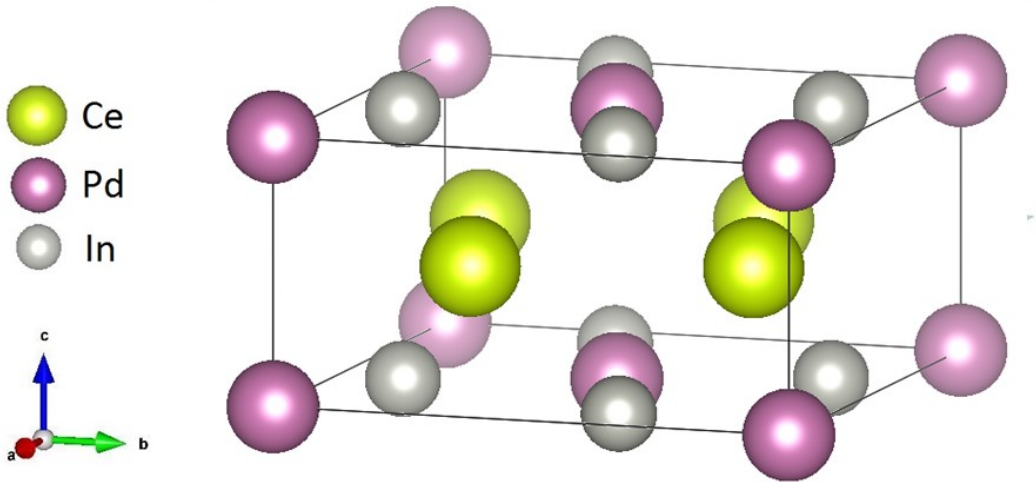

Figure 4.1: Crystal structure of Ce_2Pd_2In (tetragonal P4/*mbm*)

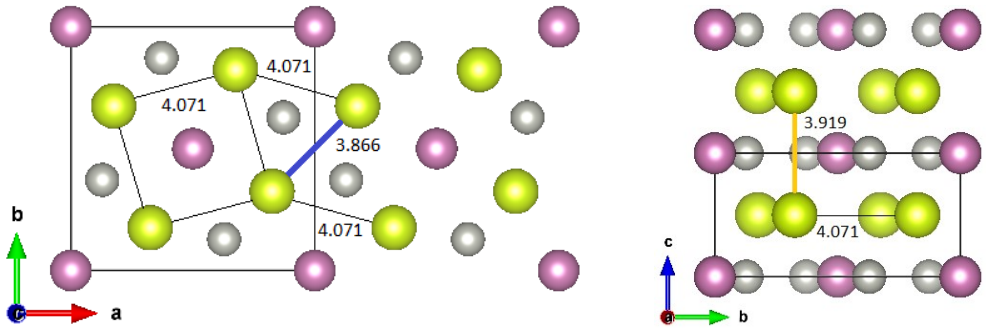

Figure 4.2: The position of magnetic nearest neighbors (Ce-Ce dimers) marked by the blue line (view along *c*) and of the second nearest neighbors – orange line (view along *a*). Distances (obtained at room temperature) are given in Å.

In combination with cryocooler, X-ray powder diffraction allowed us to investigate the temperature dependence of lattice parameters.

Figure 4.3 shows the evolution of diffraction patterns of Ce_2Pd_2In with temperature. We can see that some peaks change their position more significantly than the others. It is the first sign of the anisotropic evolution of lattice parameters. At the angle $2\theta = 103.5°$, highlighted in the figure, there is present the peak that cannot be attributed to the diffraction on studied crystal. It originates from the diffraction on sapphire Al_2O_3 which is used in the diffractometer as the pad for the sample. The region of this peak was excluded from fitting.

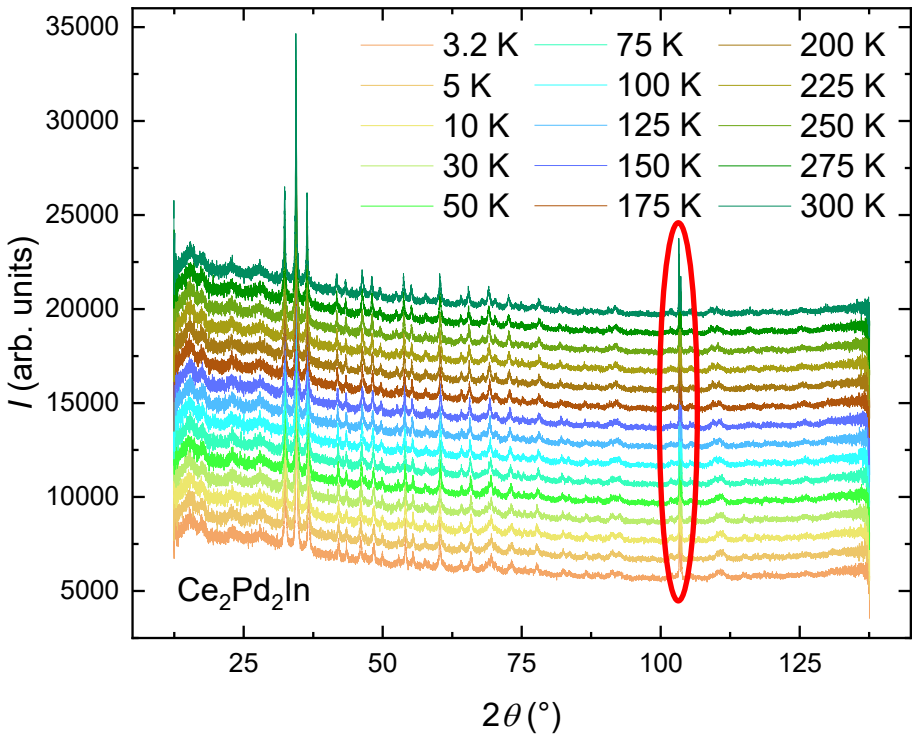

Figure 4.3: Diffraction patterns in different temperatures between 3.2 K and 300 K, red highlighted region corresponds to the diffraction on sapphire used as the pad in the diffractometer, patterns were shifted by $I = 1000$ for higher lucidity

The results of fitting are summarized in Figures 4.4 and 4.5. Expected strong anisotropy of temperature evolution of the lattice parameters *a* and *c* was confirmed. While dimension of the longer basal lattice parameter *a* decreases with temperature, perpendicular *c*-parameter is getting longer, however the changes are approximately 2-times smaller compared to parameter *a*. Temperature evolution between 3.2 and 300 K is shown in Figure 4.4. Figure 4.5 shows detailed region around the magnetic phase transitions. It is not possible to observe any effect of the transitions on the lattice parameters due to low resolution and scatter of the estimated data. In some compounds, interaction of magnetic ions in ordered state is high enough to cause the significant

change of lattice parameters at the temperature of phase transition. As we did not reveal this behavior, we can judge that the magnetostriction effect is small.

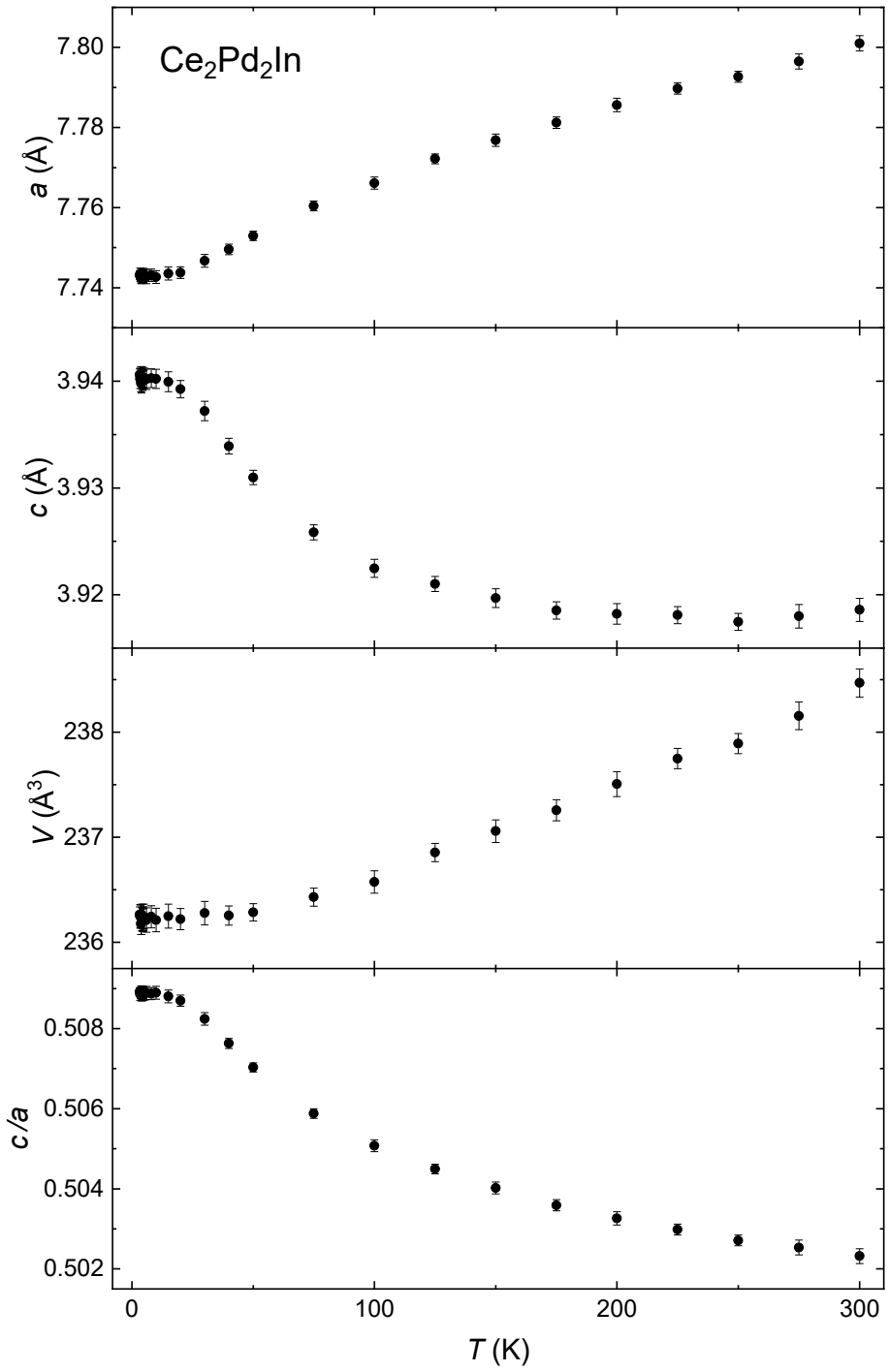

Figure 4.4: Temperature dependence of lattice parameters obtained by low temperature X-ray diffraction

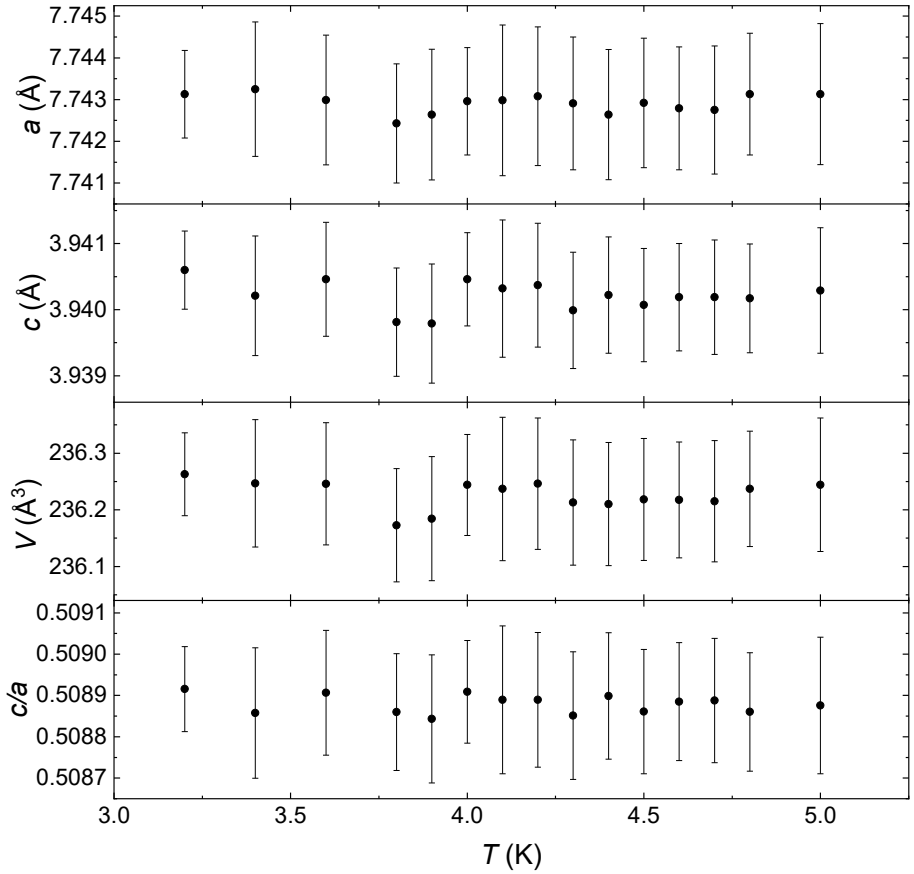

Figure 4.5: Temperature dependence of lattice parameters in the region around magnetic phase transitions

From the measured low-T XRD data, we have also investigated the evolution of distance between the nearest magnetic ions – Ce in our case. At room temperature, the Ce ions lying in basal plane form a square motif formed by Ce dimers as it is shown in Figure 4.2. The Ce-Ce distance in these dimers is also the shortest Ce-Ce distance in the compound. The second nearest neighbor lies in another Ce plane sheet, the distance is thus equal to lattice parameter *c*. Because this parameter is increasing while temperature decreases, the distance is getting longer. On the other hand, lattice parameter *a* is decreasing with cooling, that's why Ce atoms within the particular plane are getting closer to each other.

4.2. Ambient pressure characterization

All experiments discussed below in individual subchapters provide important physical information. Measured properties are also influenced by the presence of magnetic phase transitions. Figure 4.6 depicts the temperature region around them. We can see that both transitions are connected with some anomaly on the curve. Vertical lines

correspond to the positions of transitions determined from the heat capacity data using the method of idealization of transition according to specific heat while maintaining the entropy (see below for more detailed explanation). Because of the second order of both transitions, the entropy of the system evolves continuously. Although the transition is not very clearly determined by the electrical resistivity curves, the transitions cause two significant breaks on the curves and also the inflex points below the breaks can be found using the derivative of the curve. Much more clear is the situation in AC magnetic susceptibility and on the magnetization data. Both of these physical properties exhibit the inflex point at the temperatures of phase transitions.

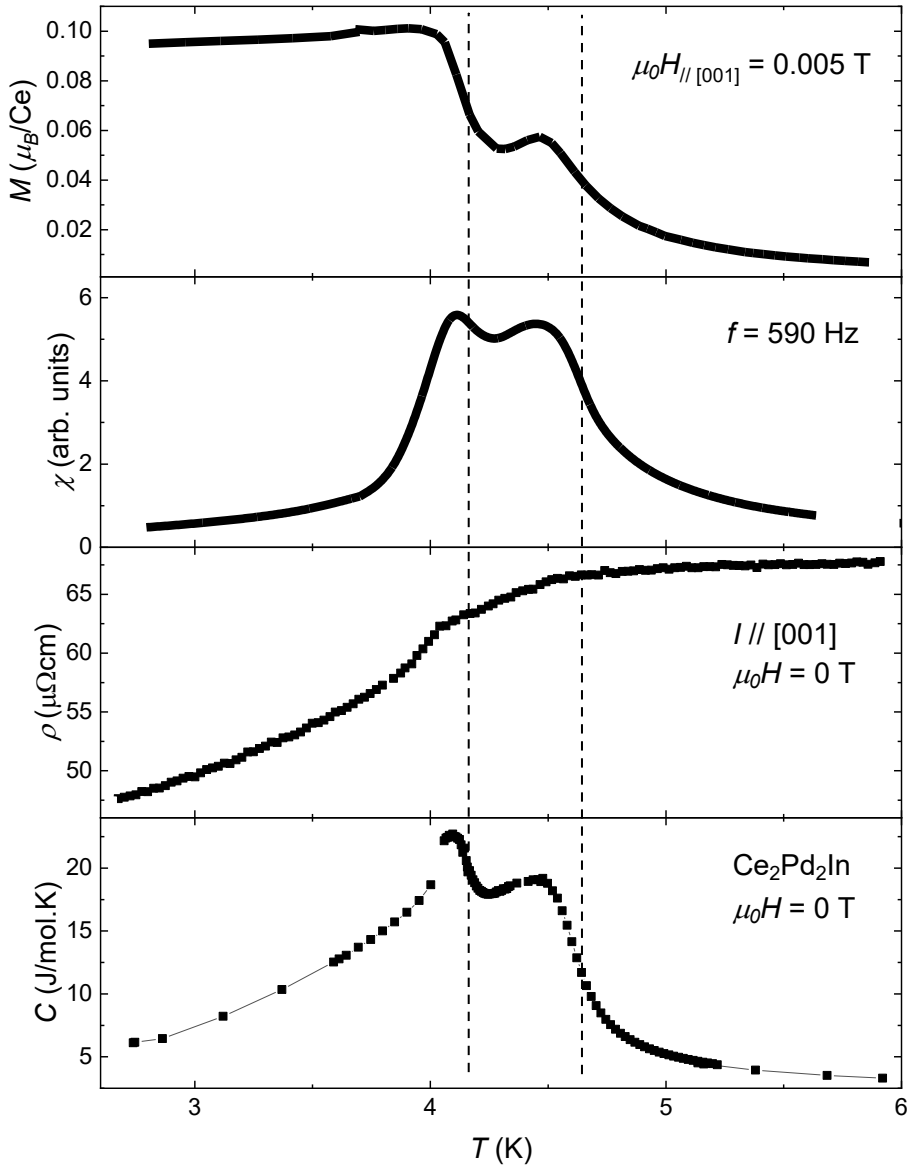

Figure 4.6: Magnetic phase transitions represented by anomalies in temperature evolution of several physical properties – magnetization, AC magnetic susceptibility, electrical resistivity and heat capacity, the vertical lines correspond to the temperatures of phase transitions determined from the heat capacity curves discussed in following subchapter

4.2.1. Specific heat

Specific heat was measured in the region between 0.35 K and 20 K. The whole curve is shown in Figure 4.7. We can see two anomalies corresponding to the magnetic transitions. In the inset, there is shown the region around magnetic transitions. These curves were measured at selected temperatures by long pulse method described in subchapter 2.4. Some pulses were overlapping, and we can see that the curves do not significantly differ for individual pulses, which indicates that the method is suitable for the measurement. In order to determine the positions of transitions, the method of idealization of transition according to specific heat while maintaining the entropy, explained theoretically in subchapter 1.4., was used. According to this method, the phase transition lies slightly above the maximum on the curve. The practical use of the method is shown in Figure 4.8 and Figure 4.9, where the details of the curves are plotted. The red lines correspond to the tangents below and above the transition. The blue line corresponds to the transition temperature, the line on such position creates the green areas (~ magnetic entropy) that are of the same surface (~ entropy conservation).

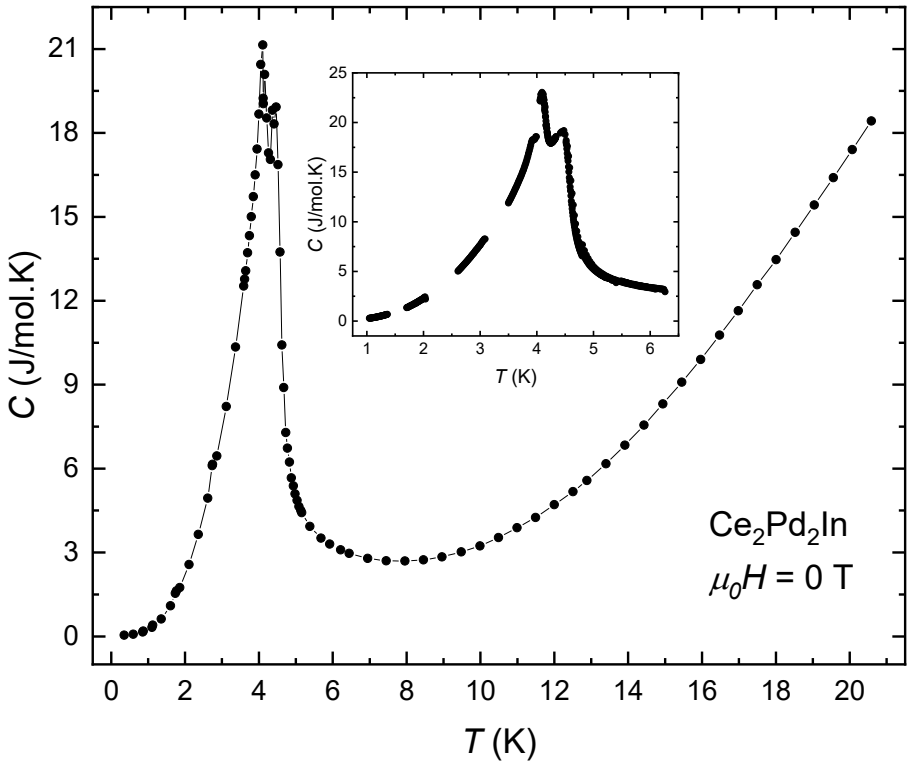

Figure 4.7: Temperature dependence of heat capacity, the inset contains the region around magnetic phase transitions measured by the long pulse method

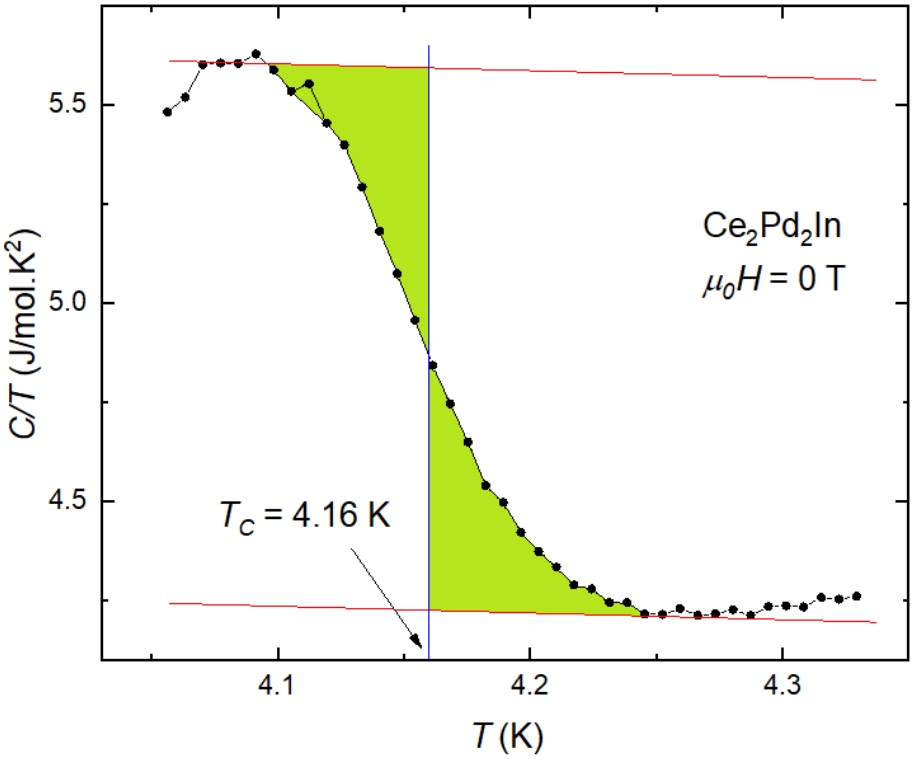

Figure 4.8: Determination of Curie temperature from the heat capacity data using the method of idealization of transition with magnetic entropy conservation. The point in the upper green area, which seems to be incorrect (probably the statistical error of measurement), was left out from the area determination

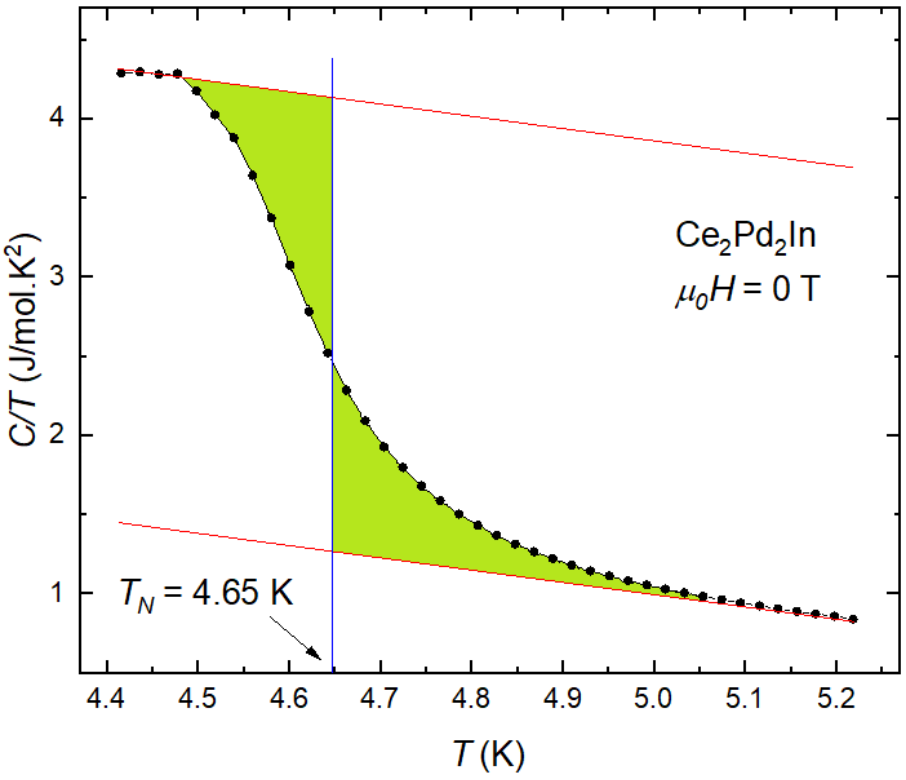

Figure 4.9: Determination of Néel temperature from the heat capacity data using the method of idealization of transition according to specific heat while maintaining the entropy

4.2.2. Electrical resistivity

Electrical resistivity of the single-crystalline sample of Ce_2Pd_2In was measured in transversal configuration of external magnetic field (applied along the [110] direction perpendicular to the *c*-axis) and current (applied along *c*-axis). We measured resistivity curve in the region allowed by PPMS (between 0.4 K and the room temperature) and then, we focused on the low temperature region around magnetic phase transitions, where also various magnetic fields were applied.

The whole resistivity curve is shown in Figure 4.10. We can observe the decreasing tendency of resistivity with lowering the temperature. Around 70 K, there is visible the significant bump, which can be probably ascribed to the spin-disorder resistivity and its changes, while the crystal field states are repopulated [40]. Around 12 K, there appears a local minimum on the curve followed by the region of two magnetic phase transitions accompanied with the large drop of the resistivity.

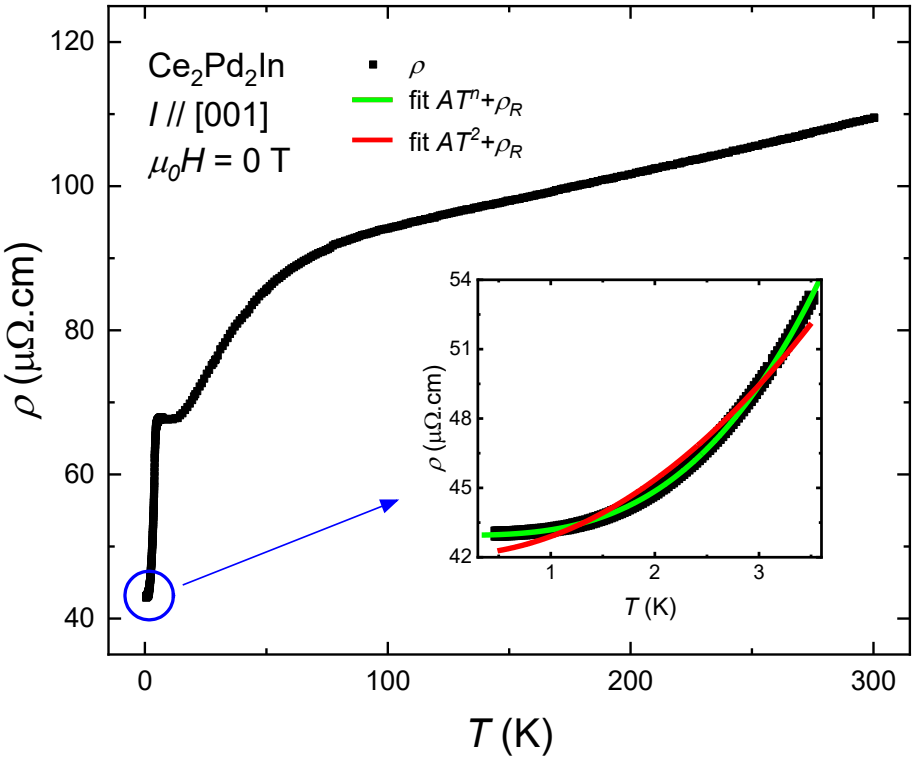

Figure 4.10: Electrical resistivity in ambient pressure and zero external magnetic field. Detail at low temperature region with fitted curves is plotted on the inset.

In the low temperature region, below the phase transitions down to He3 temperatures, the curve was fitted by $\rho = AT^n + \rho_R$ (1.26). As it is shown in the inset of Figure 4.10,

the best fit was obtained for $n = 3.01(1)$, which is against the expectation of the fermi-liquid behavior with $n = 2$. Cubed dependence on temperature was observed in several valence fluctuating Eu based systems [2]. On the other hand, in $CeIr_2Si_2$, which also exhibits valence fluctuations, the low temperature resistivity obeys typical T^2-dependence [45]. Fixing $n = 2$, as the typical value for Fermi-liquid behavior, leads to much worse fit. In both cases, the residual resistivity ρ_R is approximately 42 μΩ. cm.

The region around magnetic phase transitions in several magnetic fields is shown in Figure 4.11. In the lowest temperatures, curves obey T^3 dependence, as it is mentioned above. Then, around 3.5 K the role of presence of phase transitions starts to be significant and two kinks appear on the curves. We can see that the curves are not significantly influenced by external magnetic field up to 0.1 T, nevertheless the anomalies connected with the transitions become less significant.

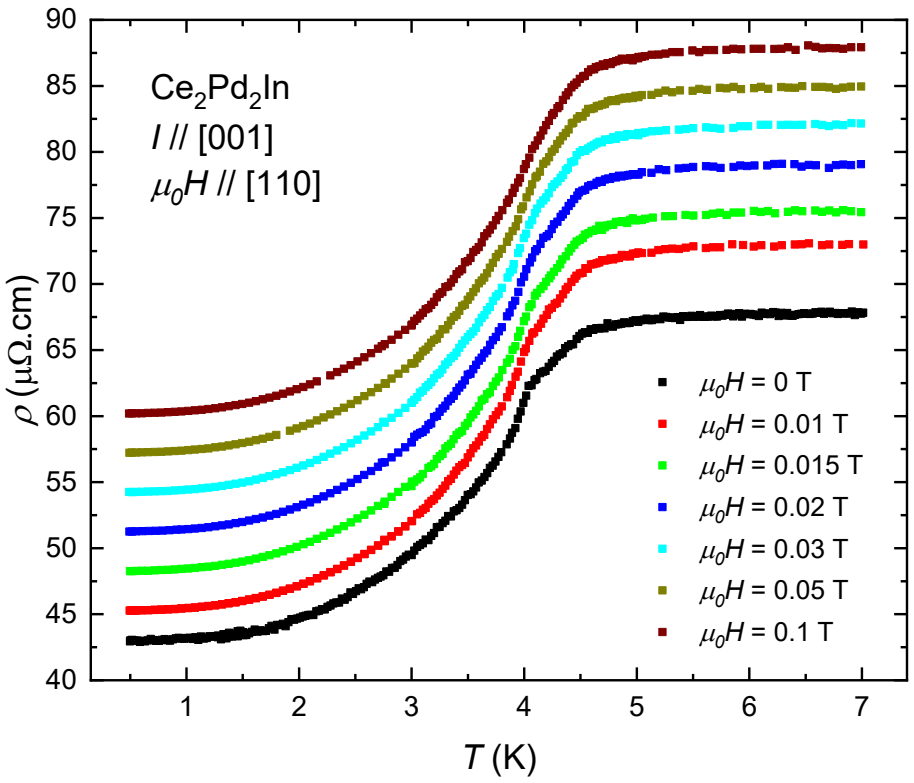

Figure 4.11: Electrical resistivity curves in the region around magnetic phase transitions for various values of external magnetic field, the curves were shifted by 3 μΩcm for higher lucidity

Magnetoresistance curves were measured too. Several temperatures (in ferromagnetic, antiferromagnetic and paramagnetic region and near the temperatures of phase

transitions) were chosen and external magnetic field up to 0.5 T was applied. A hysteresis is present in the ferromagnetic region. As the temperature is approaching to T_C, this hysteresis is getting narrower. In the antiferromagnetic and paramagnetic region, the hysteresis vanishes. In terms of the shape of the curves, the curves are convex below the transitions, it has got the wave-like shape around the transitions with presence of an inflex point, while the curves are concave in the whole measured region at higher temperatures corresponding to the paramagnetic state.

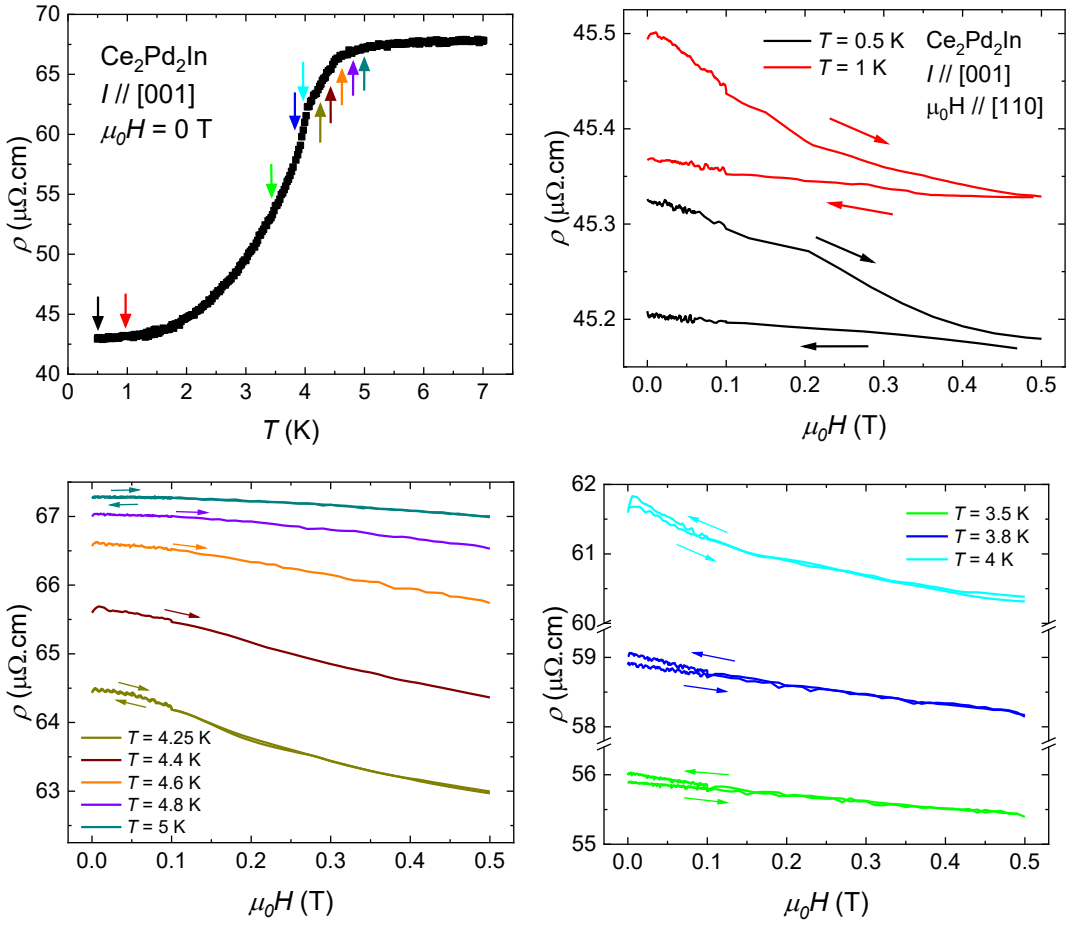

Figure 4.12: Magnetoresistance curves at selected temperatures (corresponding temperatures are marked by the arrows of particular color in the first graph)

4.2.3. DC magnetization

Magnetization was investigated in the temperature region between 2 K and 350 K with external magnetic field applied along two directions – along [110] and along the [001] direction. A strongly anisotropic behavior was observed. The *c*-axis was verified to be the easy axis of magnetization. Following Figures 4.13-4.21 summarize the magnetization data for both directions of external magnetic field.

Temperature dependence was first measured in the paramagnetic region. Data can be recalculated to the magnetic susceptibility using equation (1.18). The results are shown in Figures 4.13 and 4.14, also the inverse susceptibility is shown in the graphs. We measured for both directions of external magnetic fields of 3 T and 6 T. The independence on the sense of temperature evolution (heating and cooling) was also checked. It serves as an indication about possible presence of a ferromagnetic phase. For both values of magnetic field, the curves are almost identical. Inverse susceptibility curves obey the linear dependence in higher temperatures, in lower temperatures, the slight deflection was observed. The data in the region above 130 K (up to 350 K) were fitted using Curie-Weiss law (1.18), which allows us to find the value of the paramagnetic Curie temperature θ_P and the effective magnetic moment μ_{eff}, according to equation (1.14). Results of fits are also shown in Figures 4.13 and 4.14 and the parameters of fits are summarized in Table 4.1. The starting point 130 K of the interval was found by fitting in several temperature intervals and looking for the first starting point above which the parameters of fit do not depend on chosen starting point.

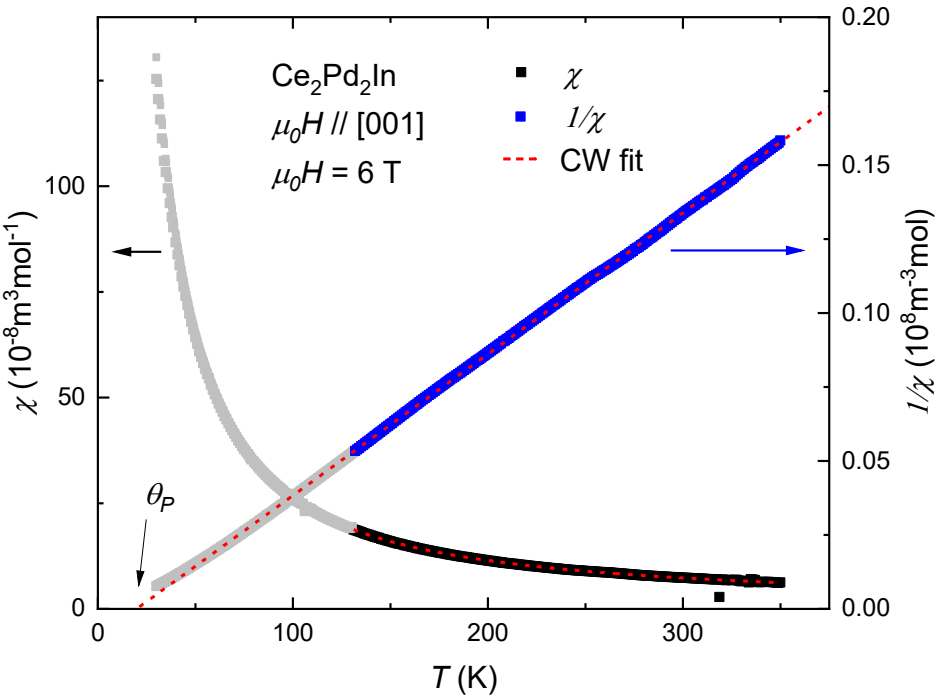

Figure 4.13: Magnetic susceptibility (left axis) and inverse magnetic susceptibility (right axis) for magnetic field applied along magnetization easy axis *c*

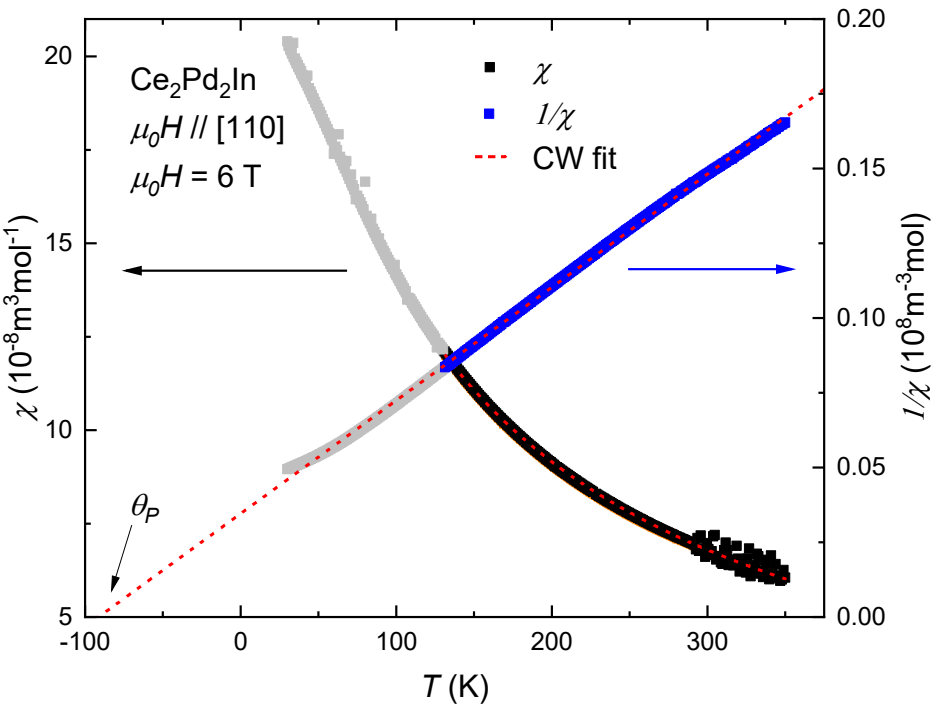

Figure 4.14: Susceptibility (left axis) and inverse susceptibility (right axis) for magnetic field applied along the basal direction [110]

Table 4.1: Curie-Weiss fitting of susceptibility data

$\mu_0 H$ direction	μ_{eff} (μ_B/Ce)	θ_P (K)
along [001]	1.80(2)	23(1)
along [110]	2.05(3)	-88(2)

Quite big difference of values obtained for different field directions can be used as a measure of uniaxial anisotropy energy $\Delta E_a = k_B \Delta\theta_P \approx 9.6$ meV, which is relatively high in Ce_2Pd_2In [40].

In terms of the region around magnetic phase transitions, the measurement of temperature dependence of magnetization was carried out in zero field cooled (ZFC) and field cooled (FC) regime for various values of external magnetic field, the results are summarized in Figures 4.15 and 4.16. All curves are flat at higher temperatures. When the temperature is approaching the transitions, the values start to grow, and the curvature appears on the dependences. Critical temperatures of phase transitions can be determined as the inflex points on the curves according to Figure 4.6 and it allows us to construct the $\mu_0 H - T$ phase diagrams shown in Figure 4.17. We can see that the choice of the regime has impact on the position of transitions – in ZFC regime they are reached at higher temperatures. Below the transitions, the behavior varies

according to the situation. In the case of field along *c*-axis and fields up to 0.015 T, magnetization reached the saturation for FC regime, whereas the curves start with the lower value of magnetization at the lowest temperatures for ZFC, then they are slightly growing before reaching the drop caused by phase transitions. For field 0.03 T, the FC curve does not reach the saturation, it is still growing at 2 K as the lowest measured temperature, the ZFC curve starts with the decreasing tendency from the beginning, the slight growth observed in lower fields is not present. For 0.1 T the situation is also different, the curves are very similar around phase transitions and the curves merge below them. Situation with field along [110] is similar, but all of the effects are more significant. Saturation is not reached for any of FC curves, the increasing tendency of ZFC curves persists up to 0.03 T and even in 0.1 T, the curves differ. In both directions of field, ZFC and FC curves are crossing below the transitions, at 3.94 K or 3.89 K for the lowest field 0.005 T applied along *c*-axis and [110], respectively. The temperature of the cross-section is decreasing in higher fields along *c*-axis and increasing for field along [110]. The fact that the FC and ZFC curves differ at low temperatures corresponding to the ferromagnetic state is the typical feature of ferromagnetic behavior. The origin of such behavior is in presence of magnetic domains. External magnetic field applied in case of FC curve plays the role in their orientation and that's why they tend to reach higher value of magnetization. In the second case, ZFC curves start from the state, where they are not oriented. This leads to the lower observed value of magnetization in the lowest temperatures. When applied external magnetic field is high enough, this effect does not play any role and both curves merge.

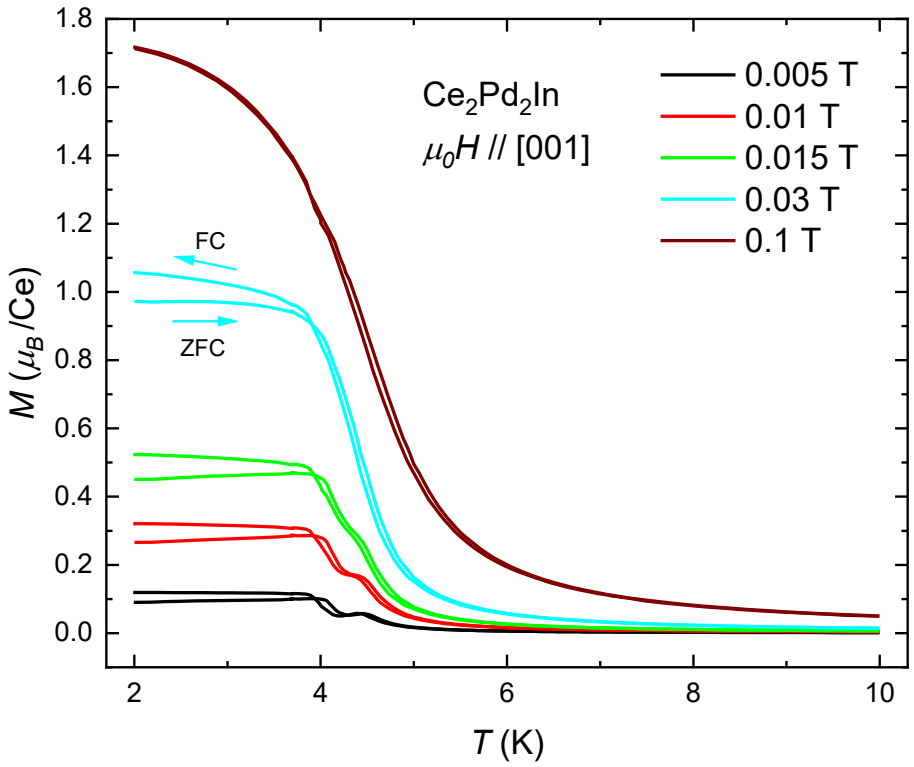

Figure 4.15: Temperature dependence of magnetization for various values of external magnetic field applied along [001] – the easy axis of magnetization

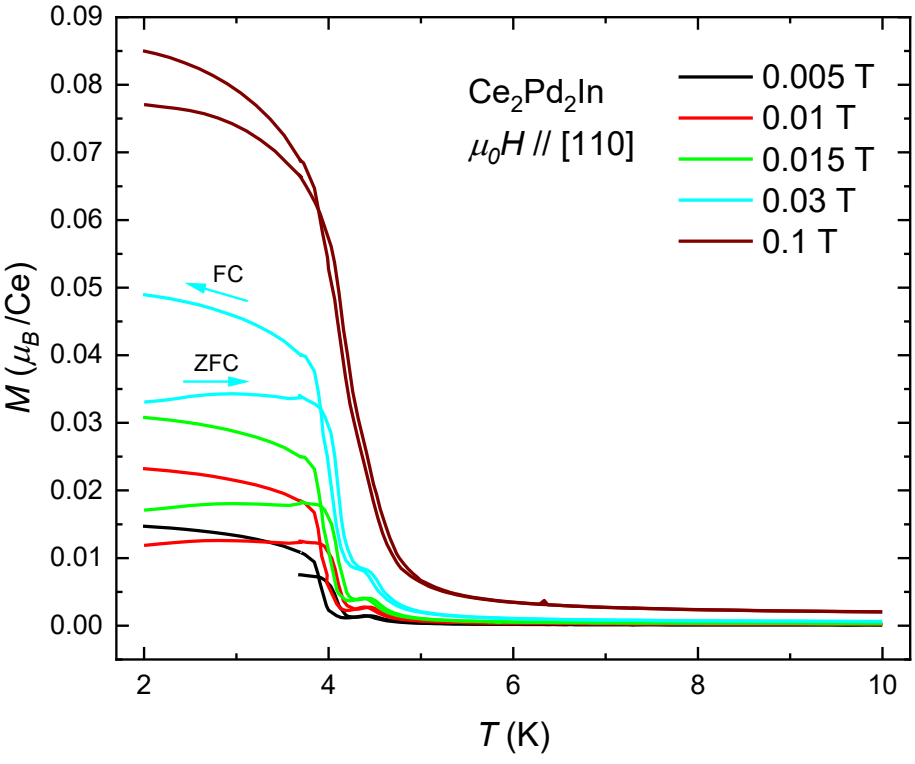

Figure 4.16: Temperature dependence of magnetization for various values of external magnetic field applied along the [110] direction

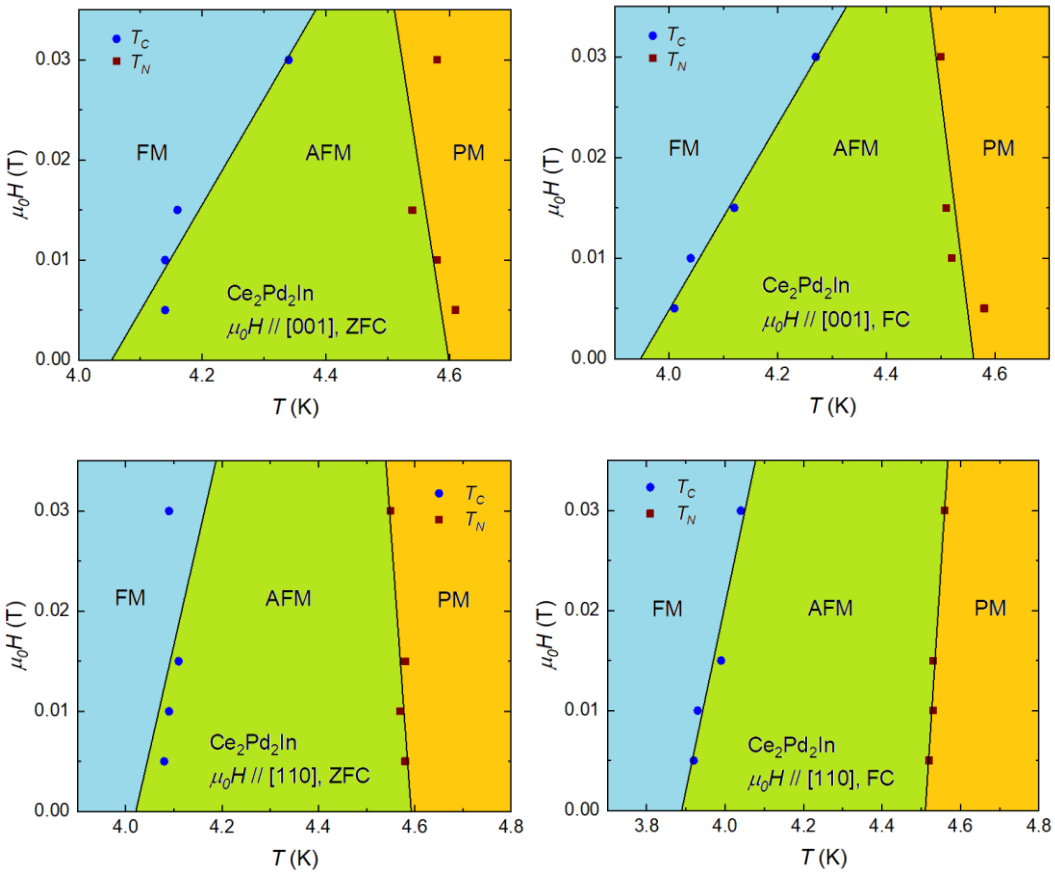

Figure 4.17: Phase diagrams of Ce_2Pd_2In ($\mu_0 H - T$), FM stands for the ferromagnetic, AFM for antiferromagnetic and PM for paramagnetic region, positions of phase transitions were determined from the magnetization data for both field directions and ZFC and FC regimes. Estimated points were fitted by linear curve to display the trend of evolution more clearly.

The magnetization curves, dependence of $M(\mu_0 H)$, were measured for systematically chosen temperatures – in ferromagnetic, antiferromagnetic and paramagnetic region and around the temperatures of magnetic phase transitions.

For field direction along the easy axis of magnetization c, we can see relatively fast saturation at the lowest measured temperature of 2 K, saturated value of magnetization is $\mu_{sat} = 1.87\ \mu_B$, which is less than the value $\mu_{Ce^{3+}} = 2.14\ \mu_B$ corresponding to the magnetic Ce^{3+} ion. The possible mechanism responsible for reduction of saturated magnetic moment are the crystal field effects and the Kondo interactions. This explanation of observed lower value is given also by Giovannini et al. [44]. In terms of the effect of temperature on the magnetization, we can see that the higher temperature was set, the higher field is needed for saturation. Figure 4.18 shows the hysteresis loops measured for various temperatures. In the inset, we can see the curves up to 2 T in detail. The region around zero field is shown in following Figure 4.19. On

the curve measured at 3.8 K (ferromagnetic state), we can observe the hysteresis closing approx. at 0.07 T. The curve from antiferromagnetic region, 4.25 K in our case, exhibits typical S-shape around the lowest fields. In paramagnetic state above temperatures of phase transitions (5 K), the curve is linear on the local scale without hysteresis.

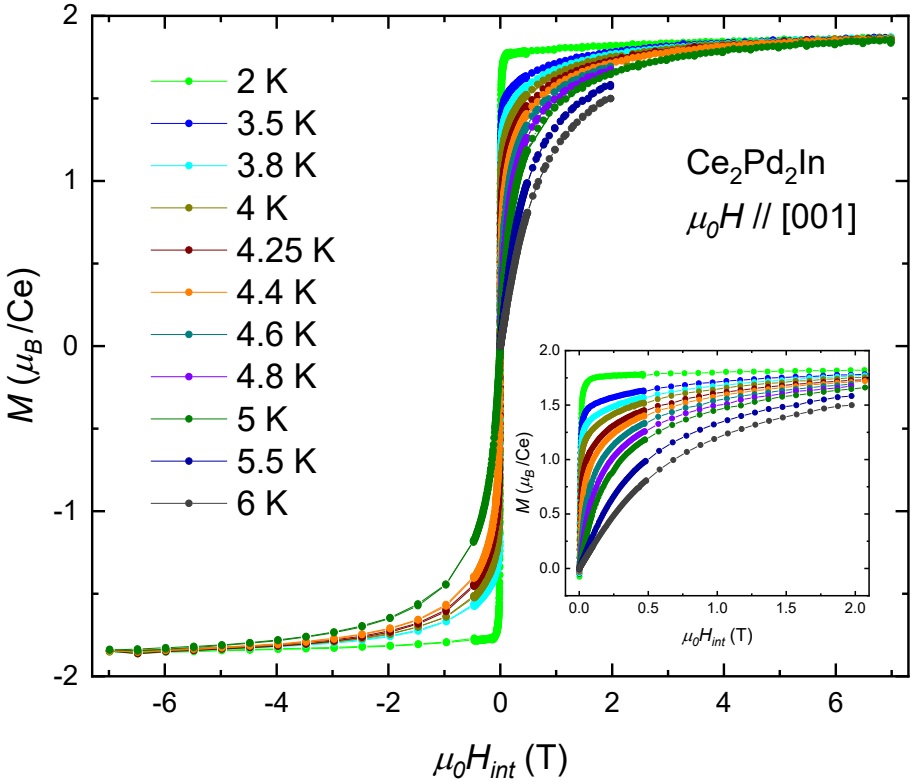

Figure 4.18: Magnetization curves for field applied along the easy magnetization axis *c* at selected temperatures with detailed depiction of region up to 2 T in the inset

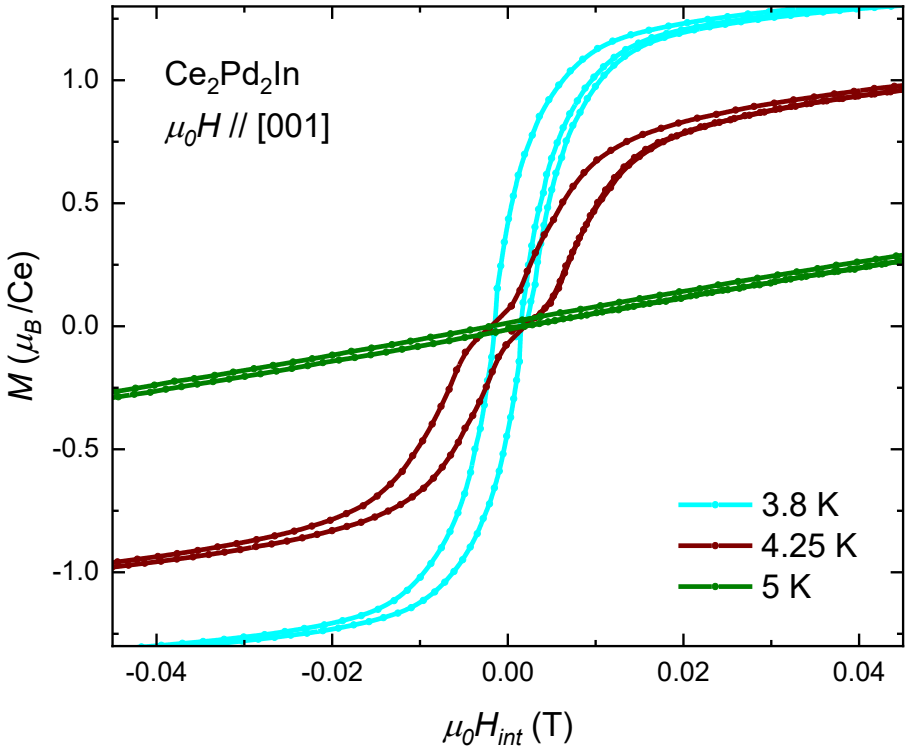

Figure 4.19: Magnetization curves for field applied along the easy magnetization axis *c* at selected temperatures in the region around zero field (3.8 K corresponds to ferromagnetic, 4.25 K to antiferromagnetic and 5 K to paramagnetic region)

The magnetization curves obtained for external field applied along the basal direction [110] are shown in following Figure 4.20. We can see that the saturation is not reached even in the highest measured magnetic field of 7 T, the values forming the curves measured at all temperatures are still growing. The detail around zero field is shown in Figure 4.21. The behavior is similar to the previous case of field along *c*-axis, the ferromagnetic curve exhibits the hysteresis, which is not, on the contrary to *c*-axis case, present on antiferromagnetic curve, at 5 K in paramagnetic region, obtained curve is linear. In terms of the width of the hysteresis loop, it is approximately ten times broader for field applied along the [110] direction in comparison with field applied along the easy axis of magnetization *c*.

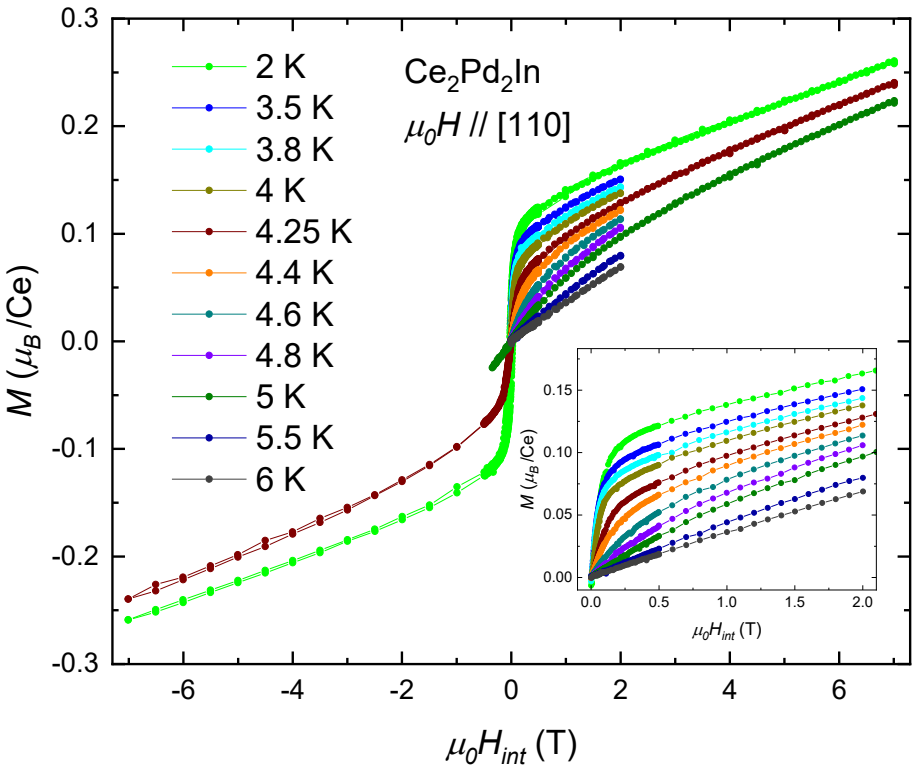

Figure 4.20: Magnetization curves for field applied along the [110] direction at selected temperatures with detailed view of the region up to 2 T in the inset

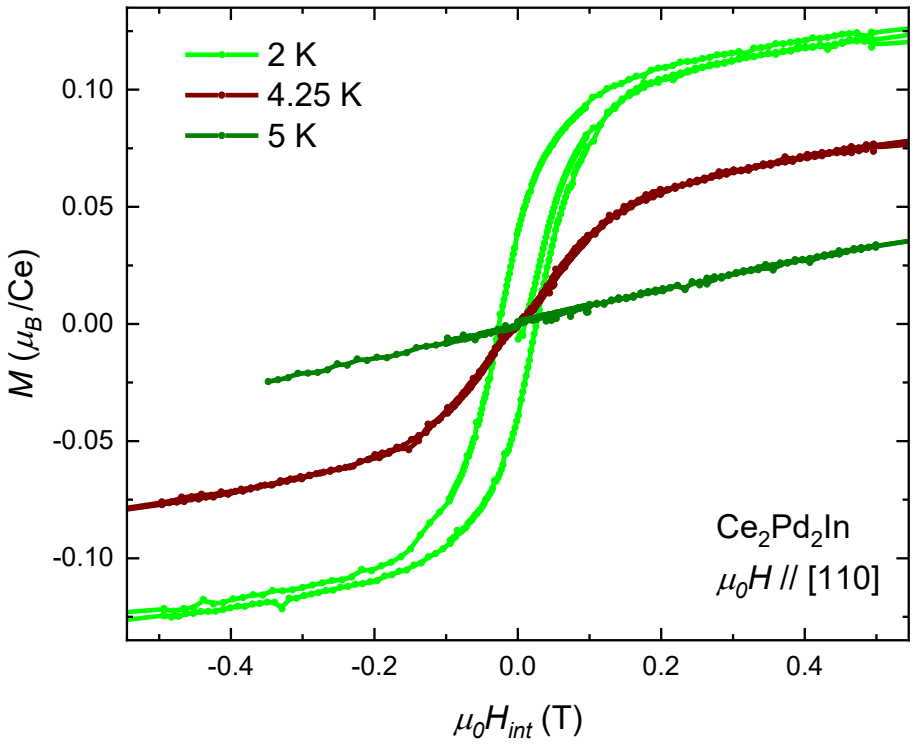

Figure 4.21: Magnetization curves for field applied along the [110] direction at selected temperatures in the low field region around zero field (ferromagnetic 2 K, antiferromagnetic 4.25 K and paramagnetic 5 K)

In both cases of field direction, external magnetic field was recalculated with respect to the demagnetization factor because of non-ideal shape of the sample. The real dimensions of the bar-shape sample were: cross section of 0.52 mm^2 and with length of 1.8 mm parallel along the crystallographic *c* direction. When the field was applied along *c*-axis, we obtained the value of demagnetization factor $D = 0.151$, which is quite small. In the second experimental setup, the field was applied along [110] direction which is parallel to the shortest side of the sample, that's why higher value $D = 0.527$ was obtained. The data presented in Figures 4.18-4.21 are already recalculated according to this factor.

4.2.4. AC magnetic susceptibility

Besides the DC magnetization, also AC magnetic susceptibility was measured. Following Figure 4.22 contains the data obtained in zero external magnetic field. We can see the curve of χ as the amplitude value of AC magnetic susceptibility. Almost same shape and values obeys χ' standing for the real part of susceptibility. The imaginary part χ'' has shown values approximately two orders of magnitude lower. The curves are affected by the presence of magnetic phase transitions. On the data of susceptibility amplitude and also on its real part, two significant anomalies appear. The inflex points correspond with the positions of phase transitions determined from the specific heat data and are marked by the vertical lines. In terms of the imaginary part of susceptibility, the vertical line intercepts the curve approximately at the inflex points. The inflex point close to the FM transition temperature $T_C = 4.16$ K is in reality lying slightly lower than the marked line.

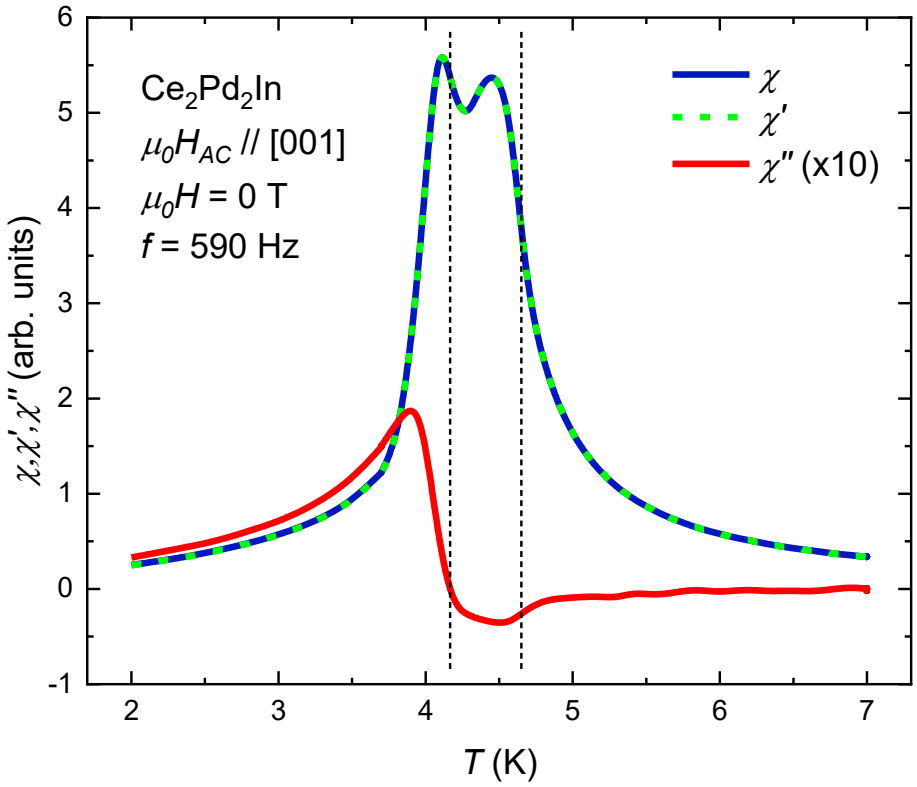

Figure 4.22: Amplitude of AC magnetic susceptibility χ, real part of susceptibility χ' and imaginary part χ''. The imaginary part is 10 times enlarged for better visibility of its changes, the vertical lines correspond to the temperatures of phase transitions determined from the heat capacity data.

As estimated above, the susceptibility results provide the information about positions of magnetic phase transitions. Also the type of the magnetic transition can be discussed according to the susceptibility results [44]. Presence of maximum both in real and imaginary part indicates the fact that below the lower transition the compound orders ferromagnetically. In contrast only the real part of susceptibility shows a maximum around the temperature of about $T \approx 4.46$ K. This fact indicates that in the region between both phase transitions, the compound is ordered antiferromagnetically.

One of the first steps in measurement of AC magnetic susceptibility was to investigate the influence of frequency on the data. From the Figure 4.23, one can see that the curves of χ and χ' (the curves are overlapping with each other as mentioned above), especially the positions of maxima, are almost independent on the chosen frequency, only a slight difference between the curves is visible below 4 K. Some frequency dependence was revealed on the imaginary part χ''. The results are shown in Figure 4.24. The maximum present below the inflex point corresponding to the Curie temperature is getting lower with increasing the frequency. On the other hand, the

minimum at the Néel temperature is visible for two lowest frequencies, the curve is almost flat for the middle values of frequency, and for higher frequencies, it is much more significant than for the previous mentioned.

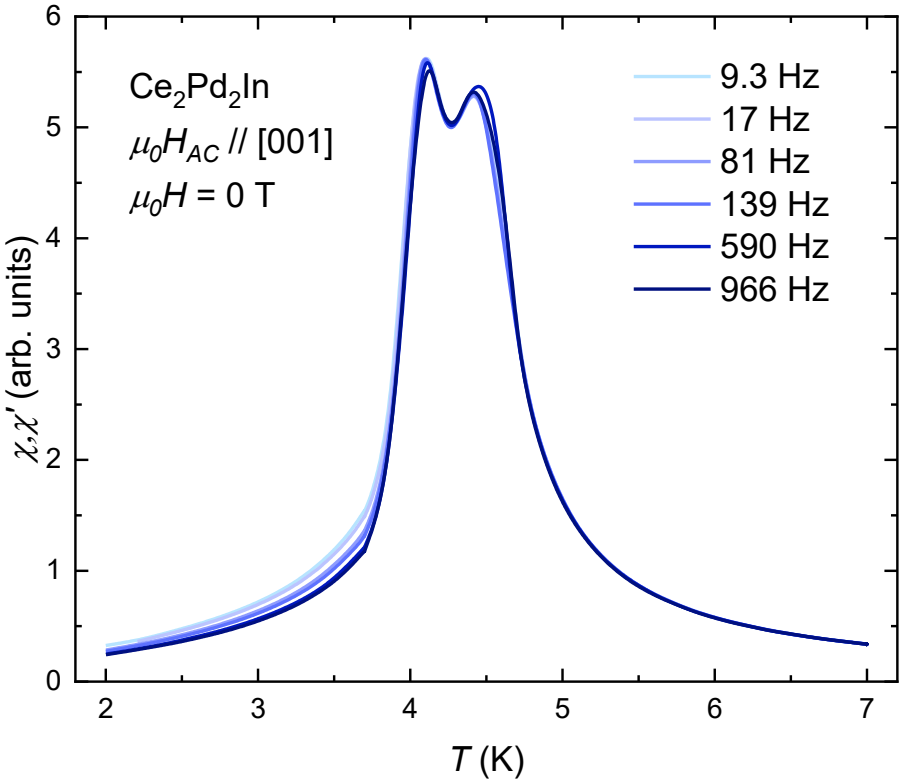

Figure 4.23: The amplitude and real part of the AC magnetic susceptibility data (χ, χ') for various values of the frequency measured at zero external magnetic field

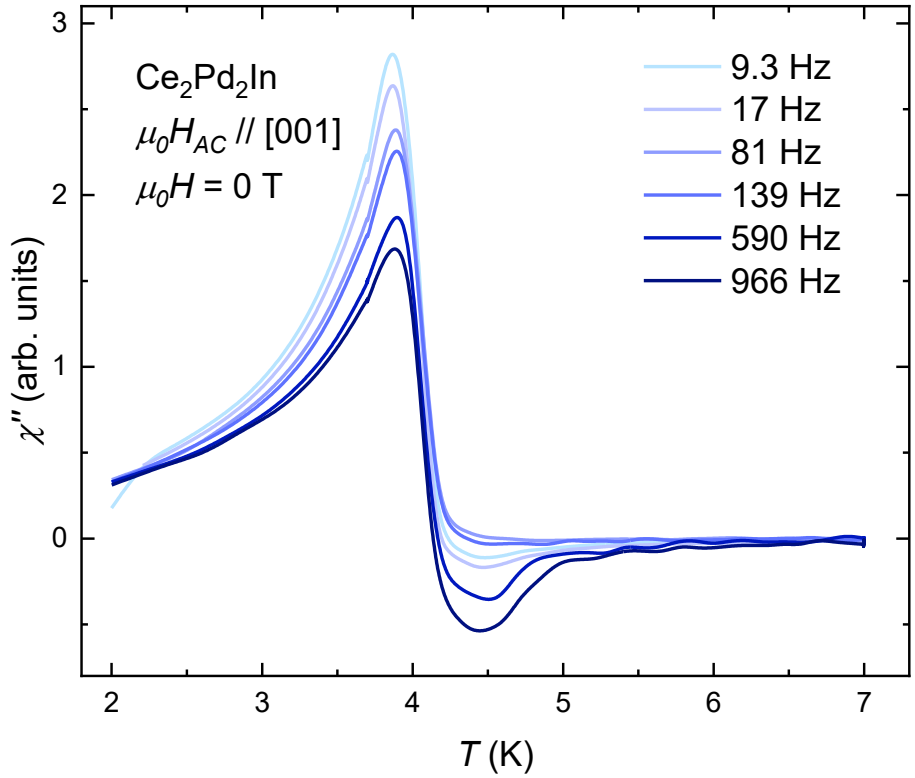

Figure 4.24: Imaginary part of the AC magnetic susceptibility data (χ'') for various values of the frequency measured at zero external magnetic field

4.3. Application of hydrostatic pressure

4.3.1. Electrical resistivity

Electrical resistivity as well as the AC magnetic susceptibility discussed in the following subchapter were measured in the double layered CuBe/NiCrAl hydrostatic pressure cell. The resistivity curves in various values of pressure are presented in Figure 4.25. Shape of the resistivity curve is sensitive to applied pressure, significant minimum around temperature of 150 K is formed with increasing the pressure. The bump at around 70 K mentioned above in the ambient pressure case is present in all pressures, but it is shifted to lower temperatures. Also the minimum above the phase transitions is present in all pressure values. The residual resistivity is higher in higher pressures. The values of resistivity at 2 K as the lowest temperature measured in all pressures are shown in following Table 4.2.

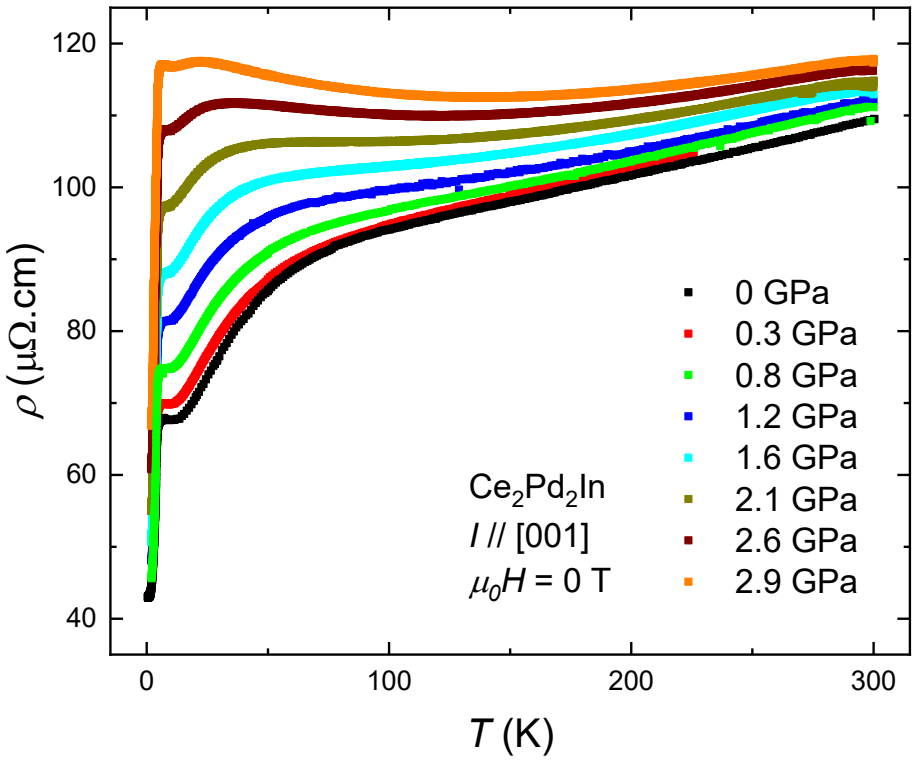

Figure 4.25: Electrical resistivity curves in pressure range between 0 GPa and 2.9 GPa and zero external magnetic field

Table 4.2: Resistivity obtained at 2 K for various values of applied hydrostatic pressure

p (GPa)	0	0.3	0.8	1.2	1.6	2.1	2.6	2.9
ρ_{2K} (μΩcm)	43(1)	44(1)	46(1)	48(1)	51(2)	55(2)	61(2)	67(2)

Following Figure 4.26 depicts the region around the phase transitions. The data are shown in the form of R_{10}/R, where R_{10} stands for the resistivity value at 10 K as the temperature lying above the transitions. In the graph there is shown the evolution of inflex point which is related to the magnetic phase transition. The real position of the transition is above this anomaly as it is discussed at the beginning of chapter 4.2. It is evident, that the antiferromagnetic transition is not affected much by the mechanical pressure. On the other hand, the ferromagnetic transition is shifted significantly to lower temperatures.

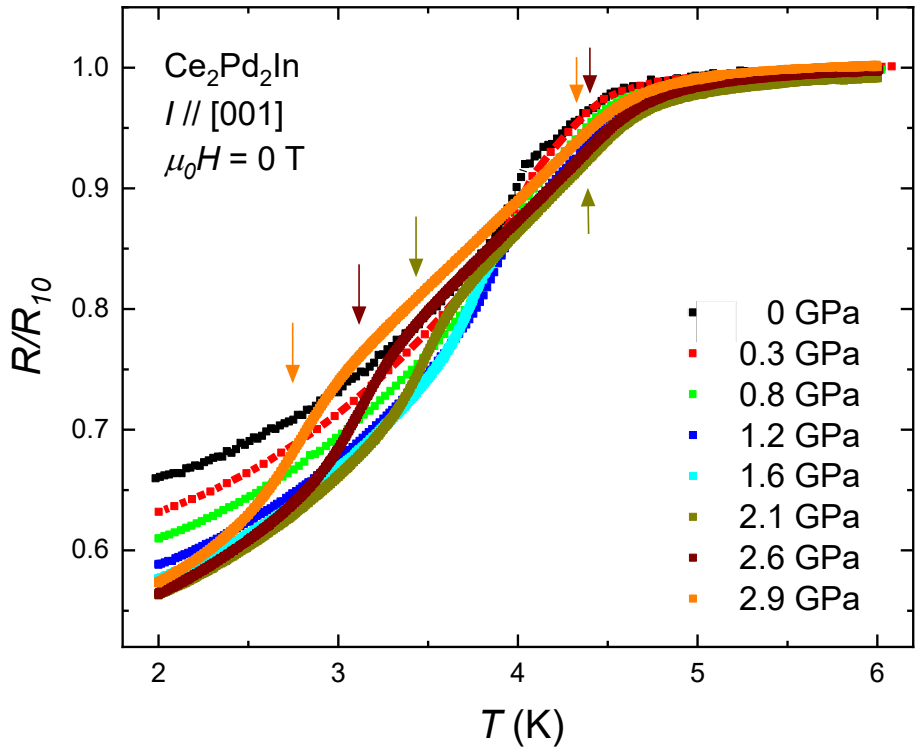

Figure 4.26: Electrical resistivity curves in pressure range between 0 GPa and 2.9 GPa and zero external magnetic field in the region around magnetic phase transitions

The influence of external magnetic field to the resistivity of the sample in various pressure points is shown in the following Figure 4.27. The influence of magnetic field is similar in all pressures, that's why only several examples are shown in Figure 4.27. We can clearly see effects of two magnetic transitions in the lowest fields. When the field is increased, the anomaly corresponding to the ferromagnetic transition is shifted to higher temperatures and the antiferromagnetic phase is suppressed.

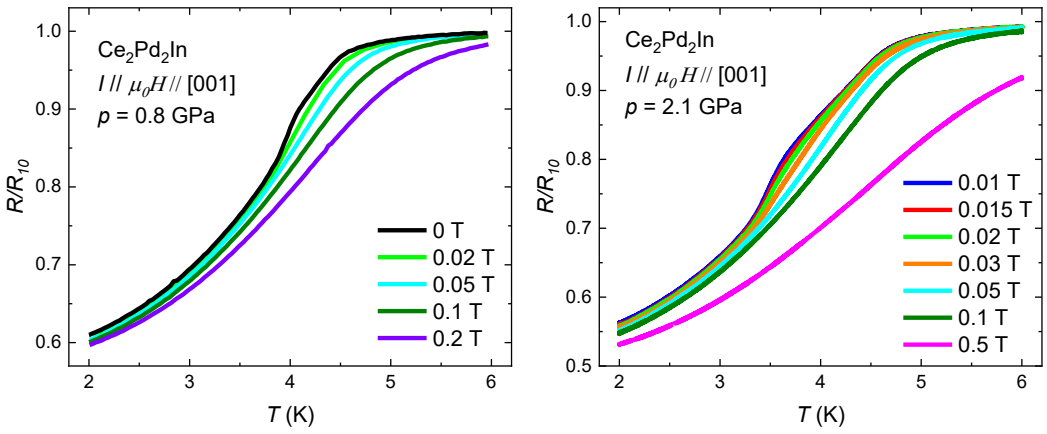

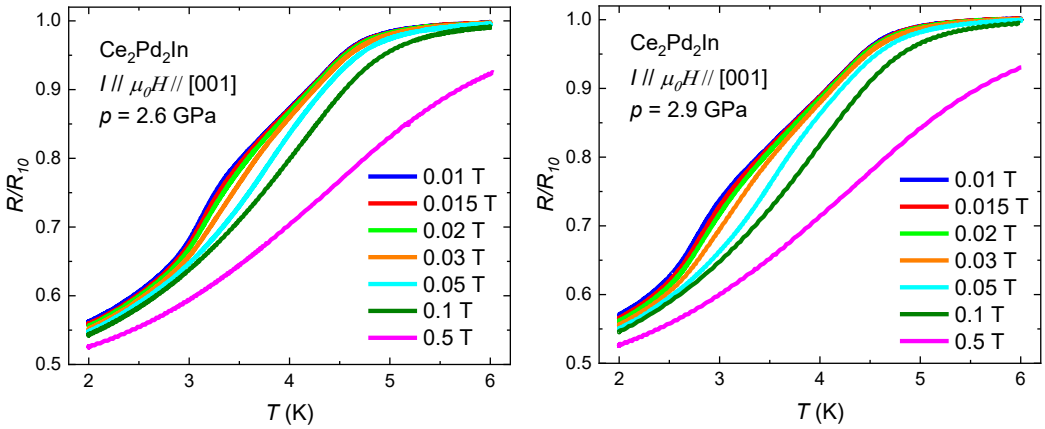

Figure 4.27: Dependence of electrical resistivity on external magnetic field measured at various values of pressure

4.3.2. AC magnetic susceptibility

As it is has been mentioned already above, the AC magnetic susceptibility was measured also in the double layer pressure cell in pressures up to 3 GPa. We obtained very similar behavior as in the ambient pressure situation. Two maxima connected with the transitions appear on the curves of susceptibility. Also here the data for susceptibility amplitude and its real part overlap, similar to ambient pressure. According to Figure 4.6, the AC susceptibility data can be used for determination of the positions of phase transitions. In accordance with determination of the transition at ambient pressure we expect the transition appearing as the inflex points lying above two significant maxima appearing on the curves. The region around the transitions is shown in Figure 4.28. The arrows of particular colors correspond here to the critical temperatures obtained at various pressures.

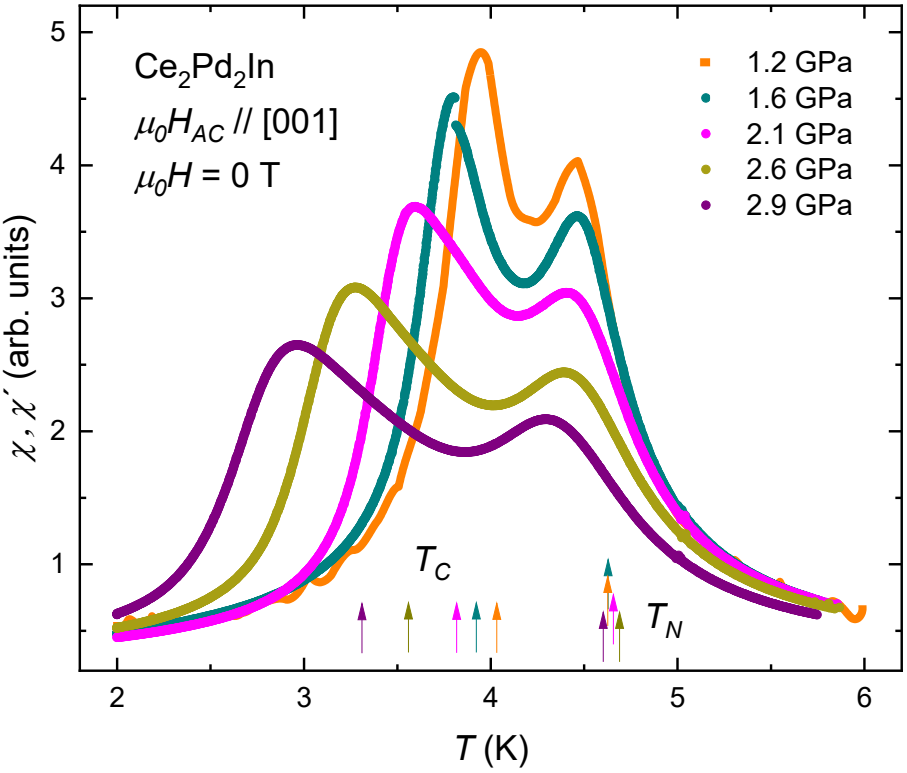

Figure 4.28: AC magnetic susceptibility (amplitude χ, real part χ') for various values of external mechanical pressure, the arrows show the positions of phase transitions (arrow colors correspond to the colors of the curves)

AC magnetic susceptibility under pressure was also measured with respect to the influence of external magnetic field. Obtained results are in good agreement with the features observed on resistivity curves. In case of zero field and field 0.01 T, two significant anomalies can be seen on the curves. For higher field, the anomaly related to ferromagnetic transition is getting broader and shifted to higher temperature as the field supports the magnetic order in the external field direction. Approximately above 0.02 T the anomalies are merging for all pressures. This is in good agreement also with magnetization data measured under ambient pressure discussed in subchapter 4.2.3. The shape of the curves is dependent on applied pressure. We can see that merging of curves for given external magnetic field is more significant in lower pressures. In higher pressure, the fact that there are two different peaks on the curves is visible up to higher fields. This can be clearly seen when we compare for example 0.015 T curves. For 2.1 GPa, the peaks are already merged, however at 2.6 GPa and especially at 2.9 GPa two anomalies can be distinguished. Similar situation was observed for 0.02 T and 0.03 T, where a borader peak is visible rather than two single peaks at

higher pressures. Above 0.05 T the antiferromagnetic phase is suppressed for all pressures.

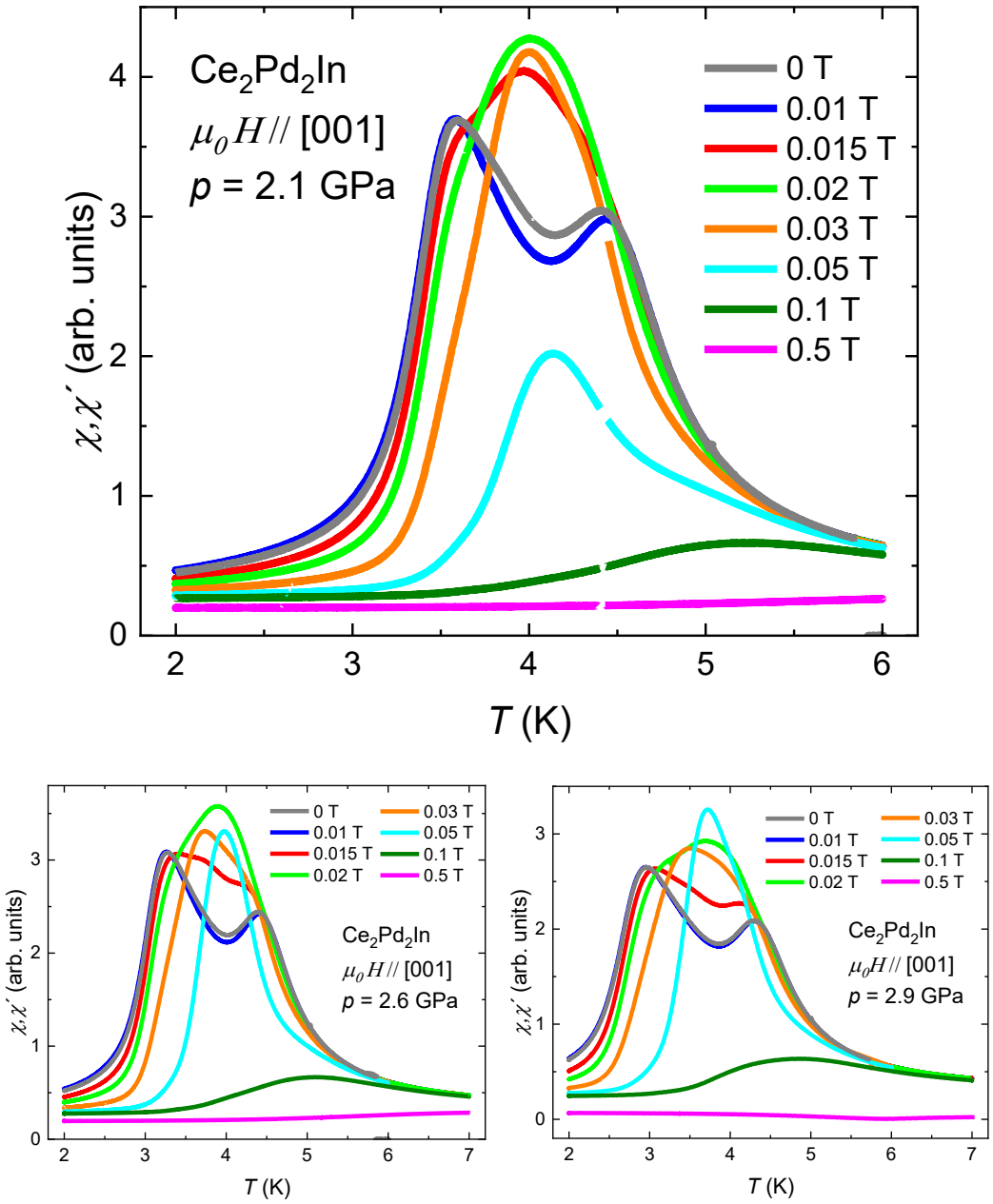

Figure 4.29: AC magnetic susceptibility (amplitude χ, real part χ') for various values of external mechanical pressure measured under the influence of external magnetic field up to 0.5 T

4.3.3. Magnetization

Magnetization was measured in CuBe pressure cell up to 1.1 GPa. As it is mentioned in chapter 2.6., pressure was determined from the temperature of superconducting transition in Pb. The magnetization measured on Pb around this transition for various

values of pressure is shown in following Figure 4.30. We can see that the values are negative which corresponds to the fact, that Pb is diamagnetic. Temperatures of phase transitions were determined as the inflex points on the curves. The resulting pressure was estimated from the known pressure dependence of T_C of lead [17] as described in subchapter 1.5.2.

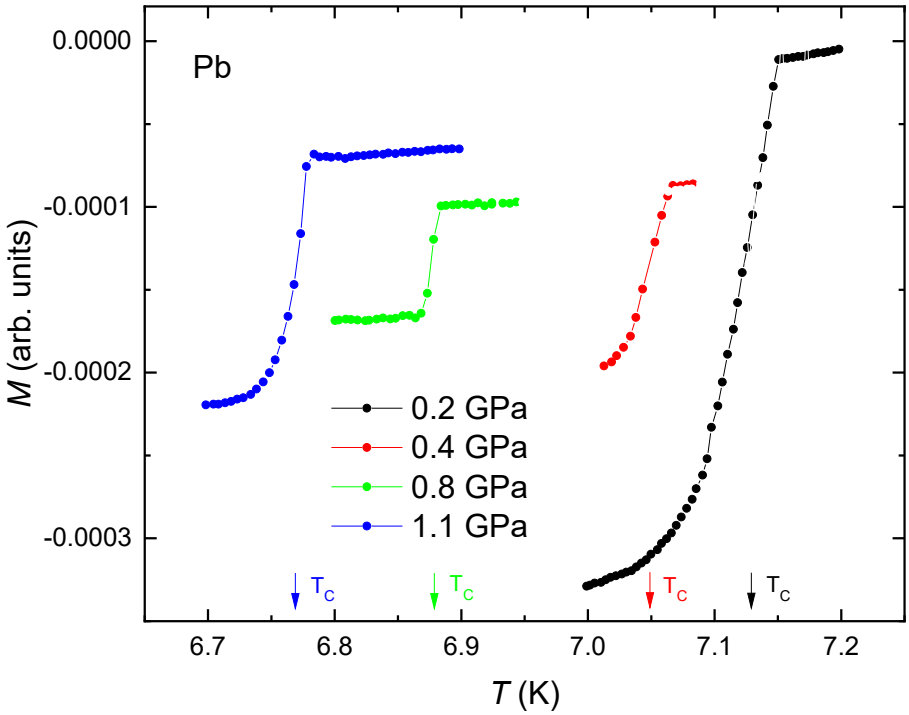

Figure 4.30: Pressure determination from position of superconducting transition observed in temperature dependence of magnetization in Pb, position of inflex point is for each curve marked by arrow of particular color

In these four pressure points, the dependence of magnetization on external magnetic field and temperature was measured. As in the case of ambient pressure characterization, the external magnetic field, which was applied along the easy axis of magnetization c in our measurement, was recalculated with respect to the demagnetization factor $D = 0.151$.

Following Figure 4.31 summarizes the evolution of magnetization with temperature for various values of hydrostatic pressure and of external magnetic field.

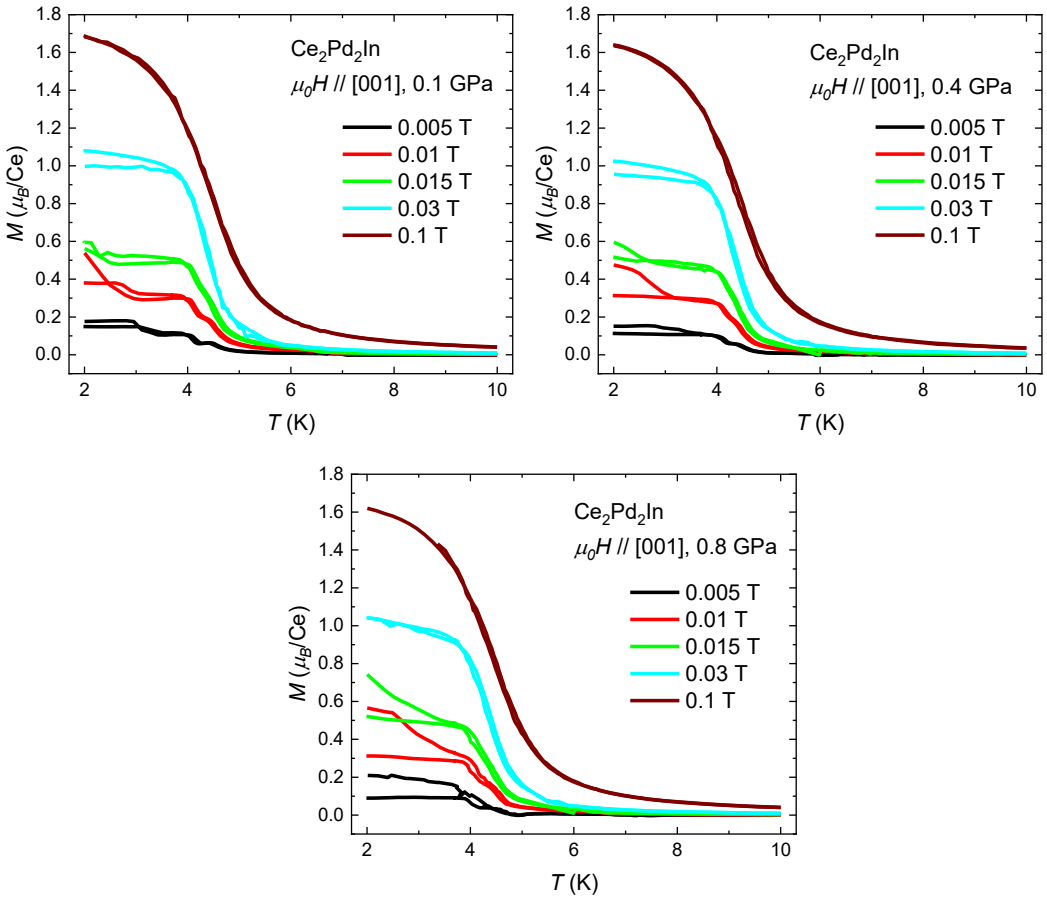

Figure 4.31: Temperature dependence of magnetization under the influence of hydrostatic pressure and various values of external magnetic field

We can see, that the behavior is very similar to that in ambient pressure – Figure 4.15. Two magnetic phase transitions are visible on the curves. For the lowest values of external magnetic field, curves have the tendency to reach the saturation value of magnetization, while for the higher field, the saturation is not reached down to the lowest measured temperature of 2 K. However, there is the significant difference in the value of magnetization at 2 K. The following table summarizes the values of magnetization at 2 K and 0.1 T for various values of applied hydrostatic pressure.

Table 4.3: Low temperature value of magnetization (2 K) in external magnetic field 0.1 T in dependence on the hydrostatic pressure

p (GPa)	0	0.1	0.4	0.8	1.1
$\mu_{2\ \mathrm{K};\ 0.1\ \mathrm{T}}$ (μ_B/Ce)	1.71(1)	1.69(1)	1.64(1)	1.62(1)	1.58(1)

It is evident, that the hydrostatic pressure leads to reduction of saturated moment. The same pressure effect was observed on the magnetization curves measured under the

influence of hydrostatic pressure and even more significant was the effect in case of uniaxial pressure (see below).

Another difference is in dependence on ZFC and FC regime. The situation is similar as in ambient pressure, in ferromagnetic region the difference between ZFC and FC curve is more significant and it has got the same explanation as mentioned in ambient pressure case.

Following graphs contain the magnetization curves measured at selected temperature from ferromagnetic (2 K), antiferromagnetic (4.25 K) and paramagnetic (5 K) region measured in dependence on applied hydrostatic pressure.

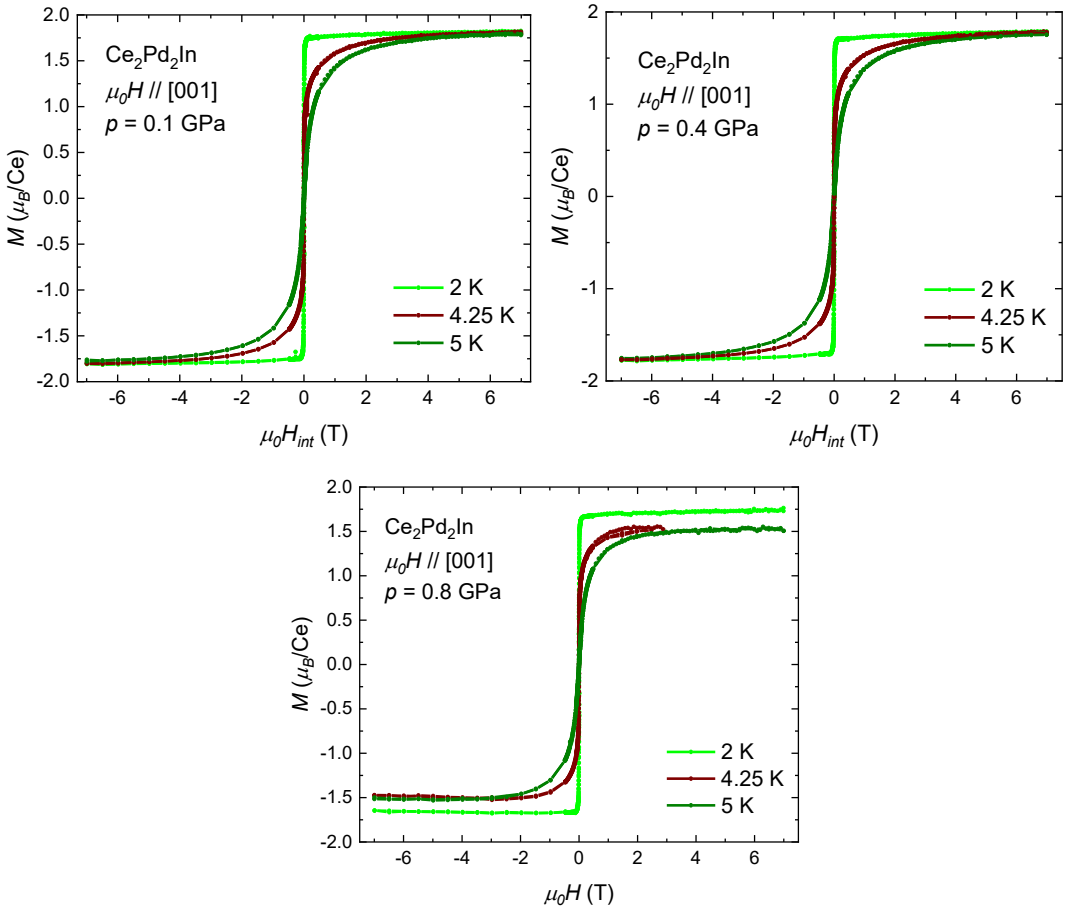

Figure 4.32: Magnetization curves measured under the influence of hydrostatic pressure at selected temperatures (2 K from ferromagnetic region, 4.25 K from antiferromagnetic region and 5 K from paramagnetic one)

We can see that the shape of the curves does not depend significantly on applied pressure. In terms of the different value reached in saturation for 0.8 GPa at 4.25 K and 5 K, it is probably caused by technical problems that occurred during the

measurement. The pressure cell froze in the chamber of PPMS and the engine ensuring the movement of the cell with sample was not able to work well. This is also the reason, why the data measured at 4.25 K do not continue above 3 T. After that the data did not have good sense.

Another difference, which is for better illustrativeness shown in following Figure 4.33, is the pressure reduction of saturated magnetic moment.

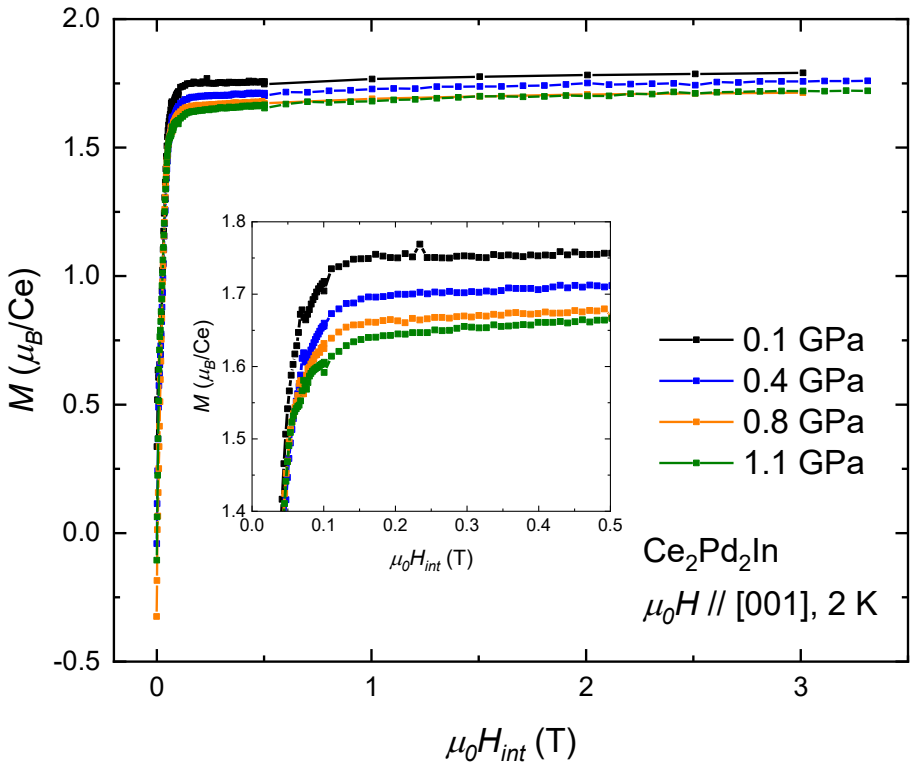

Figure 4.33: Magnetization curves measured at 2 K for various values of hydrostatic pressure, the colors are chosen with respect to the pressure values in the uniaxial pressure experiment discussed below

Table 4.4: Saturated magnetization in dependence on the value of hydrostatic pressure

p (GPa)	0.1	0.4	0.8	1.1
μ_{sat} (μ_B/Ce)	1.75(1)	1.70(1)	1.66(1)	1.64(1)

4.3.4. Phase diagram

All experiments discussed in previous three subchapters including measurement of electrical resistivity, AC magnetic susceptibility and DC magnetization under pressure provide the information about pressure evolution of the positions of both observed magnetic phase transitions. As it is already mentioned in particular subchapters, suitable for determination the critical temperatures are especially the magnetization

measurements and the measurements of susceptibility. On both of these quantities, two inflex points can be found at temperatures of transitions. Determined positions allow us to construct the $p - T$ phase diagram shown in Figure 4.34. This diagram shows evolution of characteristic temperatures of both magnetic transitions (Curie temperature T_C for the ferromagnetic and Néel temperature T_N for antiferromagnetic one) in dependence on hydrostatic pressure. Applied pressure affects both phase transitions. We can see the systematic suppression of ferromagnetic phase, the antiferromagnetic phase remains to significantly lower temperature under applied pressure, while the temperature of antiferromagnetic transition is not affected a lot. For estimation of total suppression of the ferromagnetic state, the extension of the experiment to higher pressure range is needed. The estimation of required pressure is given in Figure 4.35 by the extrapolation of the pressure dependence of Curie temperature to the zero temperature. This way we obtained $p_{T_C \to 0} \approx 5$ GPa. To confirm this estimation a higher pressure application is needed.

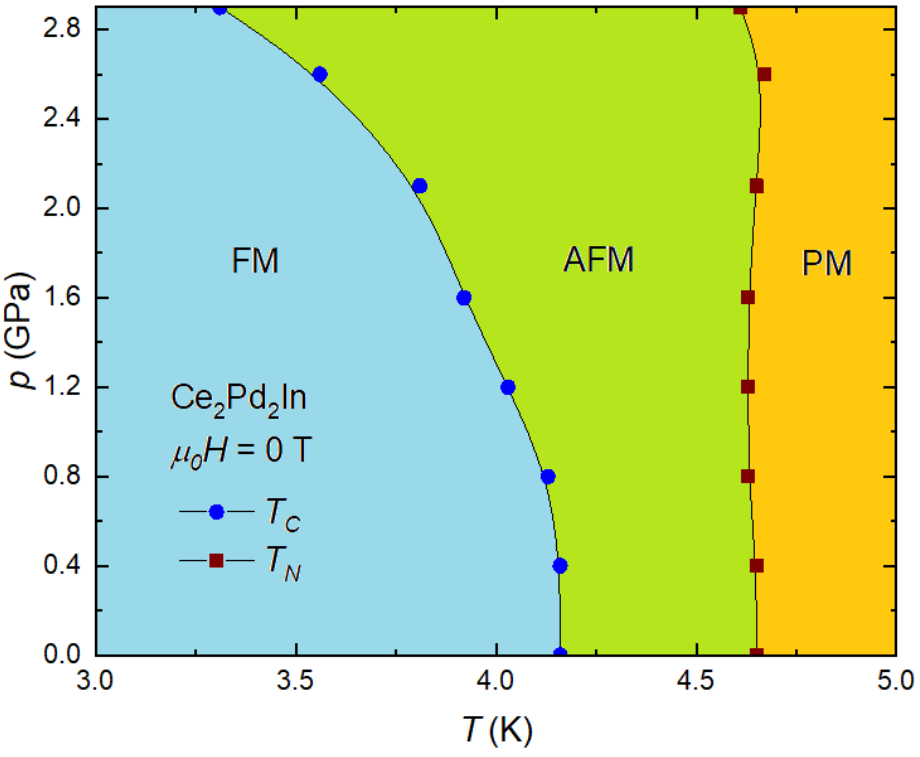

Figure 4.34: Phase diagram showing the evolution of critical temperatures of magnetic phase transitions in dependence on applied mechanical pressure

In following phase diagram, there is shown the extrapolation of the dependence of Curie temperature on applied pressure already mentioned above. It provides only the

rough estimation of the pressure required for the total suppression of ferromagnetic state. In terms of the Néel temperature, no prediction can be done from measured data, because of the fact that until the highest measured pressure of 2.9 GPa, the changes of T_N is not significant.

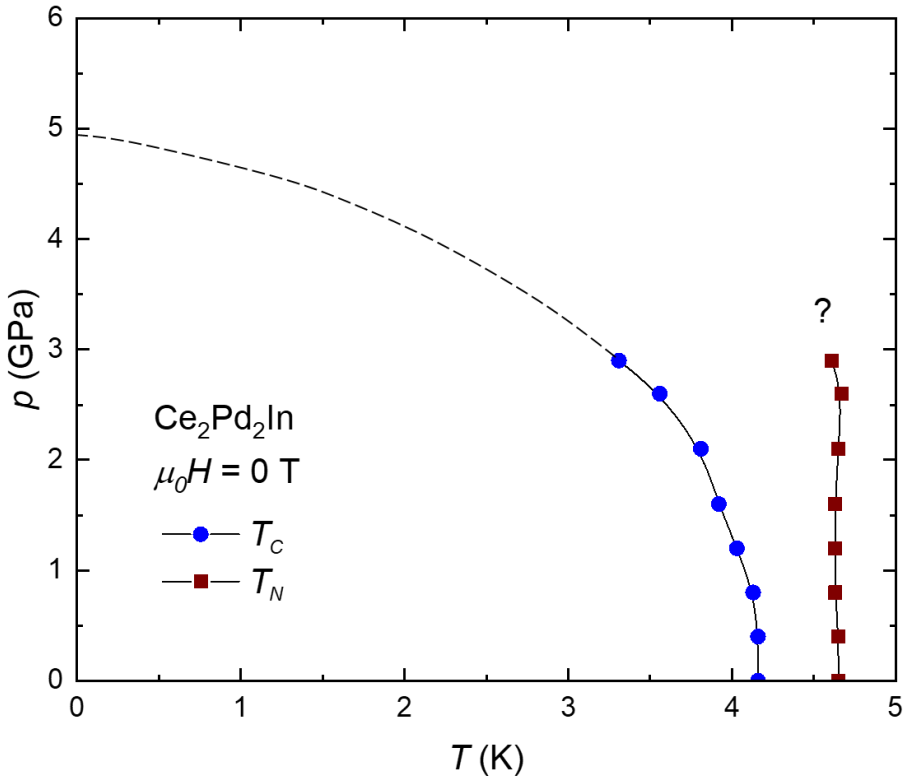

Figure 4.35: Extrapolation of $p - T$ phase diagram to $T_C = 0$

4.4. Application of uniaxial pressure

The uniaxial pressure was applied along the *c*-axis in CuBe uniaxial pressure cell, which allows us to measure the magnetization in MPMS. External magnetic field was applied along the easy axis of magnetization *c*.

Figure 4.36 contains magnetization data in dependence on temperature and applied pressure. These curves allow us to study positions of phase transitions (as the inflex points on the curves) and to construct $p_{uniaxial} - T$ phase diagrams as it is shown in Figure 4.37. When comparing the individual graphs one can see the saturation in the lowest temperature according to expectation from ambient pressure experiment. Here, the higher external magnetic field is applied, the higher saturated magnetization is reached. Magnetic field also affected the shape of the curves, for the highest 0.1 T field, it is very difficult to find the position of antiferromagnetic transition, the

antiferromagnetic phase is being suppressed by field. This is well visible on the phase diagrams below these graphs.

On the other hand, the uniaxial pressure up to 0.5 GPa does not affect the shape of the curves significantly. Also the positions of phase transitions do not change significantly under applied pressure. However, the slight tendency to systematic increase of the Curie temperature can be seen.

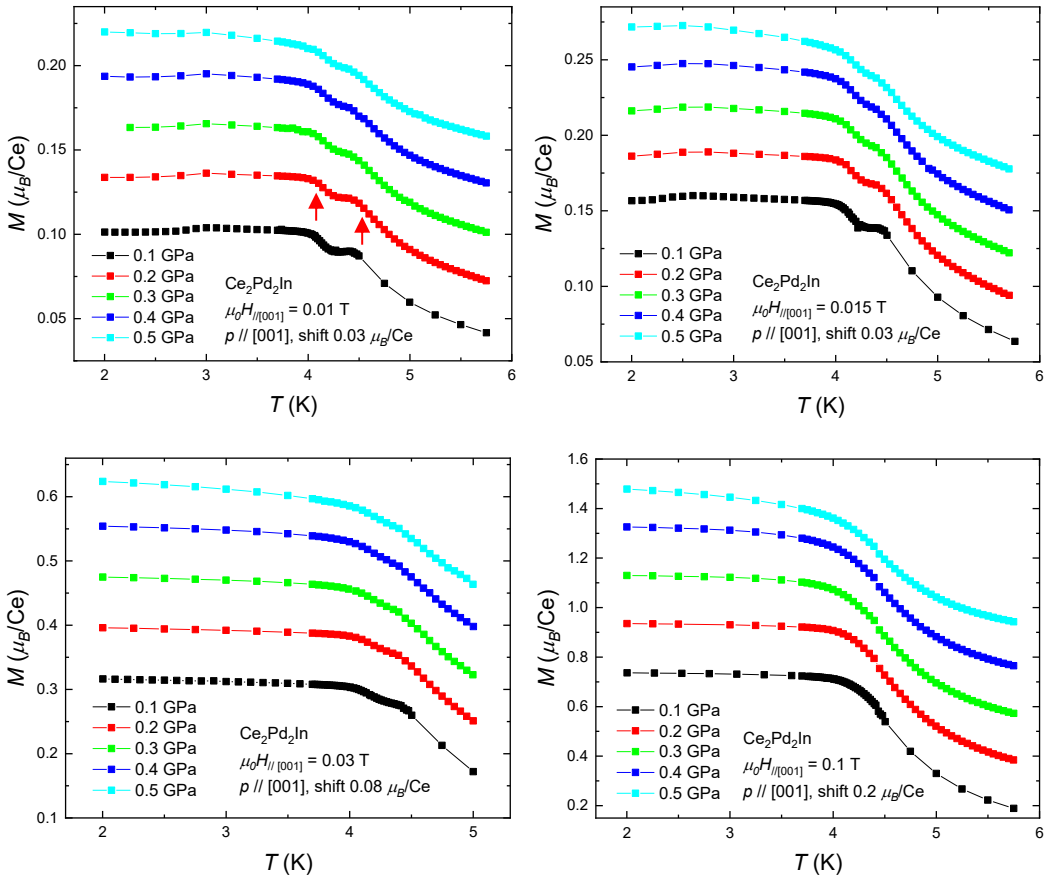

Figure 4.36: Temperature dependence of magnetization under the influence of uniaxial pressure and various values of external magnetic field, curves were shifted for higher lucidity by the value mentioned in each graph. As an example, the positions of transitions (inflex points) are marked by the arrows on one curve.

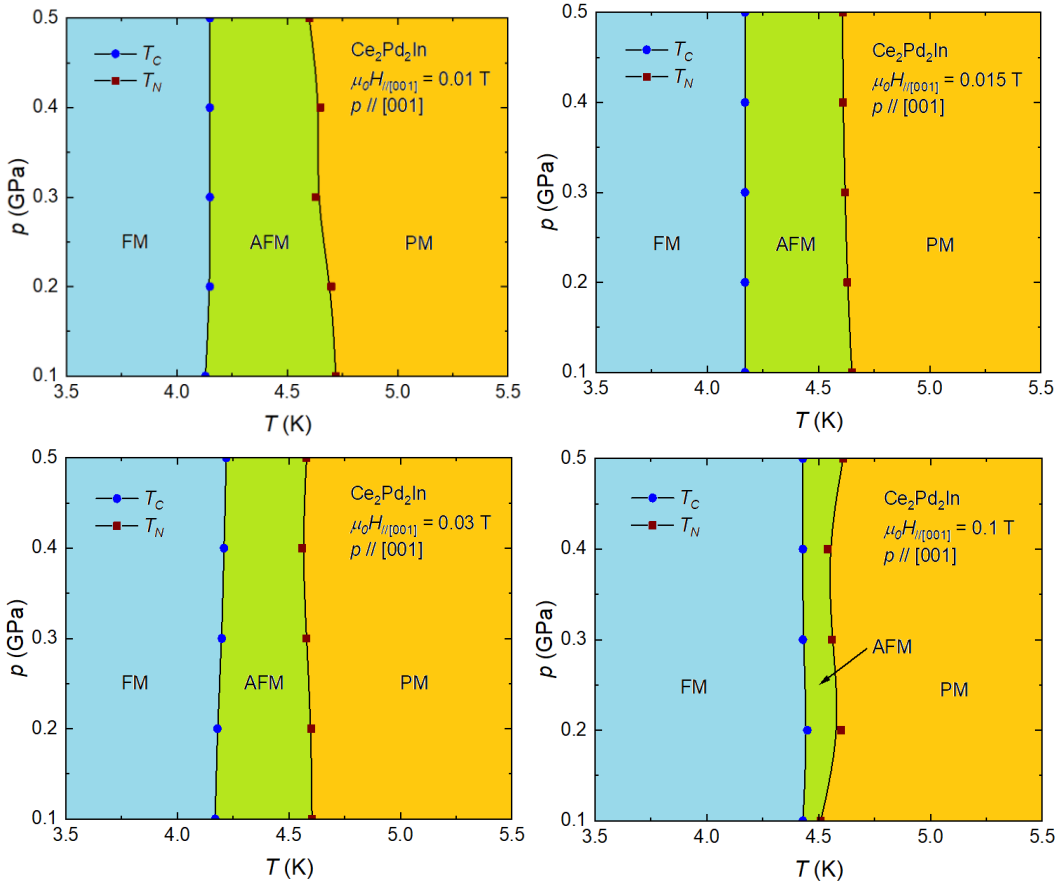

Figure 4.37: Uniaxial p - T phase diagrams of Ce_2Pd_2In. FM stands for the ferromagnetic, AFM for antiferromagnetic and PM for paramagnetic region.

The magnetization curves measured in uniaxial pressure and the temperature of 2 K are shown in Figure 4.38. Magnetization reaches the saturation quickly and we can see that the saturation value of magnetization is decreasing with increasing the uniaxial pressure. The values of $\mu_{0.5\,\mathrm{T}}$ are summarized in Table 4.5. The behavior of saturated magnetization is similar to the hydrostatic pressure case, but the effect of uniaxial pressure is larger. The saturation at $p_{uniaxial} = 0.4$ GPa is near the value obtained for $p_{hydrostatic} = 0.8$ GPa, μ_{sat} reached at $p_{uniaxial} = 0.5$ GPa is much lower than the value found for the highest applied hydrostatic pressure 1.1 GPa.

In higher magnetic fields, the decreasing tendency of the curves measured in the pressure was observed. This is caused by the diamagnetic contribution of the pressure cell originating in the CuBe alloy and other components of the pressure cell. The diamagnetic contribution to the total magnetization is significant in higher fields, where the moment of Ce is constant. That's why the correction was done and the

contribution of pressure cell was subtracted. Data in the following have been already recalculated.

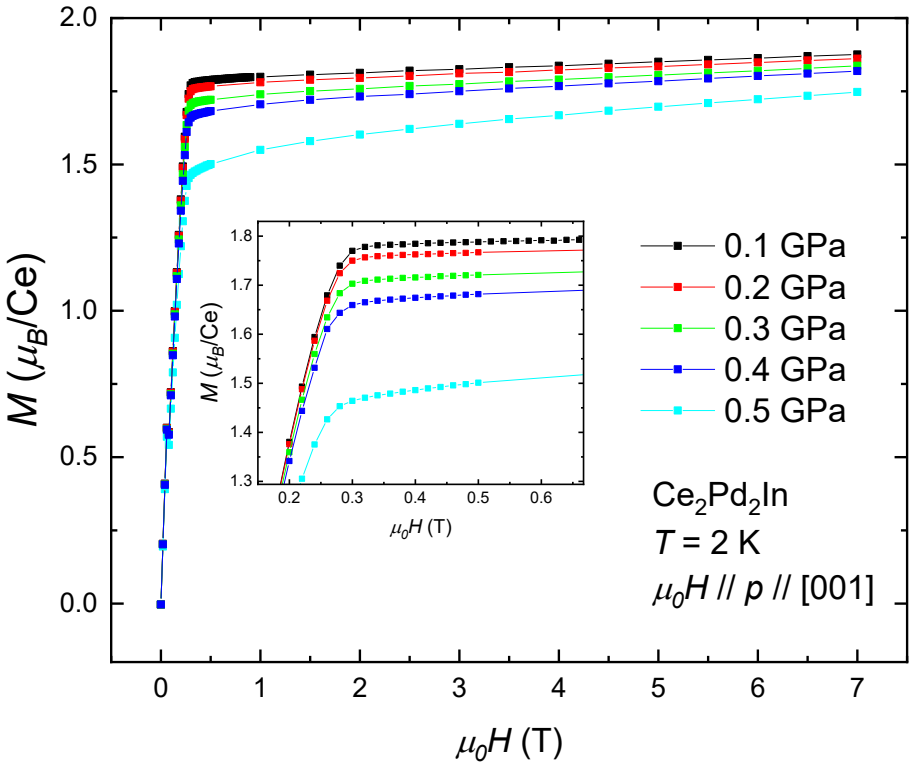

Figure 4.38: Magnetization curves measured in uniaxial pressure

Table 4.5: Magnetization at 0.5 T in dependence on the uniaxial pressure value applied along *c*-axis

p (GPa)	0.1	0.2	0.3	0.4	0.5
$\mu_{0.5\,\mathrm{T}}$ (μ_B/Ce)	1.78(1)	1.75(1)	1.71(1)	1.67(1)	1.49(2)

4.5. Discussion

Measurements of transport and magnetic properties were carried out on single-crystalline sample of the prism-like shape with the longest dimension along crystallographic *c*-axis and with shorter dimensions oriented along [110]. Our research is the continuation of systematic study of Ce_2Pd_2In compound. The sample used for our study originates from the same Czochralski crystal growth as the samples discussed by Klicpera et al. [40], which allows us to take into account the previous results, compare and verify our measurements. However, some differences were found, which will be discussed below.

The X-ray powder diffraction was carried out on powder polycrystalline sample and revealed strong anisotropy of crystal lattice temperature evolution. The diffraction pattern was analyzed, and indices of all peaks were can be ascribed to P4*/mbm* space group. However, one peak present at the angle $2\theta = 103.5°$ cannot be attributed to the diffraction on studied crystal. It originates from the diffraction on saphire which is used in the diffractometer as the pad for the sample.

Temperature dependence of crystal lattice provides the information about evolution of distances between the nearest magnetic neighbors. The distance between Ce atoms in our case is responsible for the resulting magnetic properties. The most typical exchange interaction for 4f intermetallic systems is RKKY interaction, which strongly depends on the distance between magnetic ions. As it has been already mentioned above, in whole temperature region from room temperature down to 3.2 K, the nearest magnetic neighbors are lying in the basal plane. On the other hand, the distance between Ce ions in different lattice plane sheets (the second nearest neighbors) is longer and the difference between these two distances is getting more significant with decreasing temperature. We can say that the basal-plane lattice parameters are softer than parameter *c* with respect to the temperature influence because the changes of *c* are approximately two times smaller than that of *a*. It is typical that the same trend will be present also under pressure, so we can expect that the hydrostatic pressure will affect more the basal direction than *c*-axis. It inspired us to carry out also the uniaxial pressure experiment with pressure applied along *c*-axis.

As it is mentioned above, some differences between our and previous results which should be explained here were found. The first one concerns the low temperature region of electrical resistivity. In previous, the fit $\rho \sim T^2$ was done [40] and Kadowaki-Woods relation was used for determination of the Sommerfeld coefficient γ. We carried out the measurement down to lower temperature (0.45 K) and found that much better fit could be obtained for $\rho \sim T^3$. This behavior is very atypical. It can be some sign of valence fluctuations [2] or the precursor of increase of resistivity below characteristic Kondo temperature which should originate from the Kondo interaction possibly present in Ce_2Pd_2In system. However, presence of this maximum was not observed down to the lowest measured temperature of 0.45 K. As it is mentioned above, the best agreement between the fit and experimental data was found for $\rho \sim T^3$. The T^2-dependence does not describe the data very well, measured curve lies above this dependence below 1 K. If we zoom the low temperature region even more, we can see, that the measured data compared to T^3 curve are lying also higher. This feature can be speculated as the precursor of the resistivity raise which should appear at some lower temperature when the Kondo effect is actually present. This speculation cannot be confirmed due to the absence of the data down to the lower temperatures.

Magnetization measurements revealed the fact that the magnetic moment in saturation is lowered with respect to that of Ce^{3+} free ion. Discussion of this observation is provided by Giovannini et al. [44]. The reduction of saturated magnetic moment is attributed to crystal field effects and the Kondo interaction.

In terms of the DC magnetic susceptibility data, a significant difference between θ_P and μ_{eff} obtained for different field direction was found. The results are in qualitative agreement with those presented by Klicpera et al. [40].

All experiments provide information about magnetic phase transitions. The accurate position was determined from the heat capacity data using the method of idealization of transition according to specific heat while maintaining the entropy. The positions at ambient pressure and magnetic field were determined as $T_C = 4.16$ K and $T_N = 4.65$ K. At these temperatures, the magnetization curve and the curve of AC magnetic susceptibility exhibit the inflex points which can be further used for determination of positions of the transitions. On the resistivity data, we can also

observe two anomalies corresponding to the phase transitions, but they are lying at temperatures below the actual positions of transitions.

The shape of obtained curves and also the values are in good agreement with the previously published data.

Investigating of critical temperatures allowed us to construct the phase diagrams. Even in low magnetic fields below 0.05 T, the anomalies corresponding to individual phase transitions are merging and the ferromagnetic order is reached at higher temperature.

Impact of the pressure is very interesting. The external hydrostatic pressure affects both observed transitions, however the changes in the Néel temperature is not as significant and systematic as in case of the Curie temperature. Under applied pressure, T_C is shifted down to the lower temperatures. Extension of the experiment to higher pressure range is needed to estimate total suppression of ferromagnetic phase. Expected pressure needed for the suppression – approximately 5 GPa – was estimated from the extrapolation of the phase diagram. This pressure range can be reached in our laboratory conditions and remains as the subject for further investigation.

The fact that the ferromagnetic phase is being suppressed may be the effect of general trend of pressure suppressing of all form of magnetism in solids. The pressure leads generally to the higher overlap of atomic wave functions and stronger bonds. This itinerant behavior is inconsistent with present of magnetism requiring localized behavior [15, 16].

On the other hand, the uniaxial pressure applied along *c*-axis does not affect the positions of magnetic transitions significantly up to the highest applied pressure of 0.5 GPa. The uniaxial pressure allows us to directly influence the lattice parameters along the particular direction. We used the pressure applied along the direction which is more rigid with respect to temperature effect. The pressure applied along this direction acts against the fact that the nearest magnetic neighbors are lying in the basal plane. It is not possible to say (due to the experimental limits) what happens with basal plane interatomic distances under the influence of uniaxial pressure applied along *c*. It is possible that the main role plays the tendency to keep the volume – in such case the basal plane is growing, or the tendency to keep the symmetry – than the ratio between

the interatomic distances remains the same in all pressures. These two scenarios can be described by different Poisson ratio of the compound with nonzero value in the first case and zero value for the constant *a*. Usual metallic materials show Poisson ratio around 0.3 and for example of almost zero Poisson ratio we can mention cork [46]. The first mentioned scenario can explain the differences in phase diagrams observed at hydrostatic and uniaxial pressure, where the uniaxial pressure does not suppress the ferromagnetic phase on the contrary to the hydrostatic one. If it is truth that the evolution of lattice with pressure is similar to that with decreasing temperature, we can expect that the Ce atoms lying in the same basal plane which represents the nearest magnetic neighbors are getting even closer under influence of hydrostatic pressure. This can lead to the increase of antiferromagnetic interaction and thus to suppression of ferromagnetic phase.

Another feature observed both in hydrostatic and uniaxial pressure is the suppression of saturated magnetic moment. Here is the effect of uniaxial pressure significantly stronger than that of the hydrostatic one.

Conclusion

This thesis is focused on the study of physical properties of selected rare earth element-based compound Ce_2Pd_2In. Detailed ambient pressure characterization in terms of lattice, electric, magnetic and thermal properties was carried out on the single crystalline sample. The main aim of the thesis was to investigate the pressure influence on physical properties. Three types of pressure cells allowing us to measure electric and magnetic properties were used to apply the hydrostatic pressure up to 3 GPa and also the uniaxial pressure up to 0.5 GPa.

In terms of the crystal structure study, the belonging to the tetragonal structure with space group P4/*mbm* was verified and the room temperature lattice parameters were found to be $a = 7.801(2)$ Å and $c = 3.919(1)$ Å. The temperature evolution of lattice parameters exhibits strong anisotropy, the evolution of the volume of unit cell is driven mainly by *a*, which is decreasing with decreasing temperature. On the other hand, *c* is increasing, but its changes are smaller.

Measurement of transport properties was carried out with respect to the crystallographic orientation of selected sample. The heat capacity and electrical resistivity down to 0.45 K was measured. Heat capacity data was used for accurate determination of magnetic phase transitions using the method of idealization of transition according to specific heat while maintaining the entropy. Electrical resistivity exhibits the bump around 70 K which can be ascribed to the spin-disorder resistivity and its changes, while the crystal field states are repopulated, around 12 K, the minimum appears on the curves which is then followed by the region of magnetic transitions. In low temperature region obeys T^3 dependence.

Magnetization measurement shown the lower value of saturated magnetization $\mu_{sat} = 1.87\ \mu_B$ (external magnetic field applied along [001]) compared to the value corresponding to free Ce^{3+} ion $\mu_{Ce^{3+}} = 2.14\ \mu_B$. This can be probably ascribed to the crystal field effects and effects connected with Kondo interactions. The phase transitions manifest themselves as the inflex points on the magnetization curves. It allows us to construct the phase diagram. We can see that even small external magnetic field (lower than 0.05 T) leads to suppression of antiferromagnetic phase.

The paramagnetic DC magnetic susceptibility provides using Curie-Weiss law the values of effective magnetic moments with respect to the field direction as $\mu_{eff}^{[001]} = 1.80(2)\ \mu_B$ and $\mu_{eff}^{[110]} = 2.05(3)\ \mu_B$ and paramagnetic Curie temperatures $\theta_P^{[001]} = 23.1(9)$ K and $\theta_P^{[110]} = -88$ K. The significant anisotropy can be used as a measure of uniaxial anisotropy energy $\Delta E_a = k_B \Delta\theta_P \approx 9.6$ meV, which is relatively high in Ce_2Pd_2In.

Application of hydrostatic mechanical pressure leads to further lowering of the saturated value of magnetization and it also significantly influence the temperatures of magnetic phase transitions, especially the Curie temperature is shifted to the lower temperatures and the antiferromagnetic region is being broadened. The pressure evolution of Néel temperature is not so significant.

As for the uniaxial pressure applied along [001], the lowering of saturated magnetic moment is even more significant. On the other hand, the positions of phase transitions are not affected a lot.

Bibliography

[1] Shah K. V. et al., *The $Yb_2Al_{1-x}Mg_xSi_2$ series from a spin fluctuation (x=0) to a magnetically ordered ground state (x=1).* Journal of Physics: Condensed Matter 2009, 21 (17), 6001.

[2] Patil S. et al., *Anomalies of resistivity and its T3-dependence at low temperatures in Eu-based valence fluctuating systems*. Solid state communications 1990, *76* (10), 1173-1176.

[3] Wohlleben D., Wittershagen B., *Resistivity anomalies due to valence fluctuations.* Advances in Physics 1985, 34 (3), 403-443.

[4] Sales B. C., Wohlleben D., *Susceptibility of interconfiguration-fluctuation compounds*. Physical Review Letters 1975, 35 (18), 1240-1244.

[5] Gumeniuk R. et al., *Valence fluctuations of europium in the boride $Eu_4Pd_{29+x}B_8$*. Journal of Physics-Condensed Matter 2016, *28* (11), 9.

[6] Iwasieczko W., Kaczorowski D., *Hydrogen insertion effect on the magnetic properties of Ce_2Pd_2In.* Journal of Alloys and Compounds 2011, *509* (5), 1384-1388.

[7] *Why is a complete octet or duplet more stable than a neutral atom?*, [online]. Quora, 18.5.2020. Available on https://www.quora.com/Why-is-a-complete-octet-or-duplet-more-stable-than-a-neutral-atom.

[8] Ashcroft N. W., Mermin N. D., *Solid state physics.* Saunders College Publishing, Philadelphia, 1976.

[9] Kittel CH., *Úvod do fyziky pevných látek*. 1. vydání, Academia, Praha, 1985.

[10] Buschow K. H. J., Boer F. R., *Physics of magnetism and magnetic materials.* Springer, Boston, 2003.

[11] Sechovský V., Prchal J., Magnetické vlastnosti pevných látek, prezentace k přednášce.

[12] Wikipedia Contributors, Kondo effect, [online]. Wikipedia, the free encyclopedia, 18.5.2020, Last change 14.5.2020. Available on https://en.wikipedia.org/wiki/Kondo_effect#/media/File:Classickondo.png.

[13] Kirkpatrick T. R., Belitz D., *Generic non-Fermi-liquid behavior of the resistivity in weakly disordered ferromagnets and clean helimagnets*. Physical review B 2018, 97(6).

[14] Eremets M., *High pressure experimental methods*. Oxford University Press, 1996.

[15] Arnold Z., *High pressure in basic and material science*. Lecture notes.

[16] Prchal J., Arnold Z., Sechovský V., Fyzika ve vysokých tlacích, prezentace k přednášce.

[17] Bireckhoven B., Wittig J., *A diamond anvil cell for the investigation of superconductivity under pressures of up to 50 GPa: Pb as a low temperature manometer*. Journal of Physics E: Scientific Instruments 1988, *21* (9), 841.

[18] Valvoda V., Polcarová M., Lukáč P., *Základy strukturní analýzy*. 1. vydání, Karolinum, Praha, 1992.

[19] Carvajal J. R., *Recent advances in magnetic structure determination by neutron powder diffraction*. Physica B 1993, 192, 55-69.

[20] *Optická versus elektronová mikroskopie*, [online]. ZFP MFF UK, Praktikum III pro OF. Úloha 31, studijní text. Available on https://physics.mff.cuni.cz/vyuka/zfp/_media/zadani/texty/txt_331.pdf

[21] Vlášková K., *Magnetic excitations in cerium compounds*. Master thesis, Charles University in Prague, Faculty of Mathematics and Physics, 2016.

[22] Quantum Design, *Physical Property Measurement System, Electrical Transport Option (ETO) User's Manual*. Fourth edition, 2013, San Diego, USA.

[23] Quantum Design, *Physical Property Measurement System, Heat Capacity Option (ETO) User's Manual*. Eleventh edition, 2004, San Diego, USA.

[24] Quantum Design, *Magnetic Property Measurement System, User's Manual*. Third edition, 2004, San Diego, USA.

[25] Aharoni A., *Demagnetizing factors for rectangular ferromagnetic prisms*. Journal of applied physics 1998, 83 (6), 3432-3434.

[26] *Calculator for magnetostatic energy and demagnetizing factor*, [online]. Parallel Finite Element Micromagnetics Package, Werner Scholz. Available on http://www.magpar.net/static/magpar/doc/html/demagcalc.html.

[27] Fujiwara N. et al., *Fabrication and efficiency evaluation of a hybrid NiCrAl pressure cell up to 4 GPa*. Review of Scientific Instruments 2007, 78 (7), 073905.

[28] *Pressure cells*, [online]. Material Properties Measurement Laboratory, Materials Growth and Measurement Laboratory. Available on https://mgml.eu/.

[29] Wikipedia Contributors, Black garden ant, [online]. Wikipedia, the free encyclopedia, 19.5.2020, Last change 17.5.2020. Available on https://en.wikipedia.org/wiki/Black_garden_ant

[30] Murata K. et al., *Pressure transmitting medium Daphne 7474 solidifying at 3.7 GPa at room temperature*. Review of Scientific Instruments 2008, 79 (8), 085101.

[31] Staško D., *Pressure media for high pressure experiments, the family of Daphne*. To be published.

[32] Kamarád J. et al., *High pressure cells for magnetic measurements – Destruction and functional tests*. Review of Scientific Instruments 2004, 75, 5022.

[33] Yokogawa K. et al., *Solidification of high-pressure medium Daphne 7373*. Japanese journal of applied physics 2007, 46, 3636.

[34] Kamarád J. et al., *Miniature uniaxial pressure cells for magnetic measurements*. High Pressure Research 2008, 28, 633.

[35] Lukachuk M., Pöttgen R., *Intermetallic compounds with ordered U_3Si_2 or Zr_3Al_2 type structure–crystal chemistry, chemical bonding and physical properties.* Zeitschrift für Kristallographie-Crystalline Materials 2003, 218 (12), 767-787.

[36] Ye L., *Electronic transport on the Shastry-Sutherland lattice in Ising-type rare-earth tetraborides*. Physical Review B 2017, 95 (17), 174405.

[37] Gordon R. A. et al., *Magnetic properties of several Ce(2)T(2)M phases with T=Ni, Pd and M=In, Sn, Pb*. Journal of Alloys and Compounds 1995, 224(1), 101-107.

[38] Kaczorowski D. et al., *Magnetic behavior in a series of cerium ternary intermetallics: Ce_2T_2In (T=Ni, Cu, Rb, Pd, Pt, and Au).* Physical Review B 1996, 54 (14), 9891-9902.

[39] Hauser R. et al., *Specific heat and electrical resistivity studies on Ce_2T_2In, T=Ni, Rh, Pt, Pd, Cu and Au*. Physica B 1997, 230, 211-213.

[40] Klicpera M. et al., *Magnetic properties of Czochralski-grown Ce_2Pd_2In single crystal.* Journal of Magnetism and Magnetic Materials 2016, 404, 250-256.

[41] Herrmannsdörfer T. et al., *Magnetic ordering in the rare-earth intermetallic compounds Tb_2Pd_2In and Ho_2Pd_2In.* Physica B: Condensed Matter 2000, 276, 702-703.

[42] Fischer P., *Antiferromagnetic rare-earth ordering in the intermetallic compounds R_2Pd_2In (R= Pr, Nd).* Journal of Physics: Condensed Matter 2000, 12 (31), 7089.

[43] Braghta A. et al., *Magnetic and thermal properties of Ce2Pd2Sn.* Journal of magnetism and magnetic materials 2008**,** *320* (6), 1141-1145.

[44] Giovannini M. et al., *Effect of nonstoichiometry on the transition from ferromagnetism to antiferromagnetism in the ternary indides $Ce_{1.95}Pd_{2+2x}In_{1-x}$ and $Ce_{2+x}Pd_{1.85}In_{1-x}$.* Physical Review B 2000, 61 (6), 4044-4053.

[45] Mihalik M. et al., *Electronic and crystal structure of α-and β-$CeIr_2Si_2$.* Physica B: Condensed Matter 2009, 404 (19), 3191-3194.

[46] Fortes M. A., Nogueira M. T., *The Poisson Effect in Cork*. Materials Science and Engineering 1989, A122, 227-232.

List of Tables

Table 4.1: Curie-Weiss fitting of susceptibility data 39
Table 4.2: Resistivity (2 K) in dependence on hydrostatic pressure 50
Table 4.3: Magnetization (2 K, 0.1 T) in dependence on hydrostatic pressure 56
Table 4.4: Saturated magnetization in dependence on hydrostatic pressure 58
Table 4.5: Magnetization (0.5 T) in dependence on uniaxial pressure 63

List of Abbreviations

RE	Rare earth
RKKY	Ruderman Kittel Kasuya Yosida
DOS	Density of states
EDX	Energy dispersive X-ray analysis
PPMS	Physical Property Measurement System
MPMS	Magnetic Property Measurement System
SQUID	Superconducting Quantum Interference Device
XRD	X-ray diffraction
AC	Alternating current
DC	Direct current
FC	Zero field cooled
ZFC	Field cooled
FM	Ferromagnetic
AFM	Antiferromagnetic
PM	Paramagnetic